Systems/Circuits

Reliable Sensory Processing in Mouse Visual Cortex through Cooperative Interactions between Somatostatin and Parvalbumin Interneurons

Rajeev V. Rikhye,[1,2] Murat Yildirim,[1,2] Ming Hu,[1,2] Vincent Breton-Provencher,[1,2] and Mriganka Sur[1,2]
[1]Picower Institute for Learning and Memory, Massachusetts Institute of Technology, Cambridge, Massachusetts 02139, and [2]Department of Brain and Cognitive Sciences, Massachusetts Institute of Technology, Cambridge, Massachusetts 02139

Intrinsic neuronal variability significantly limits information encoding in the primary visual cortex (V1). However, under certain conditions, neurons can respond reliably with highly precise responses to the same visual stimuli from trial to trial. This suggests that there exists intrinsic neural circuit mechanisms that dynamically modulate the intertrial variability of visual cortical neurons. Here, we sought to elucidate the role of different inhibitory interneurons (INs) in reliable coding in mouse V1. To study the interactions between somatostatin-expressing interneurons (SST-INs) and parvalbumin-expressing interneurons (PV-INs), we used a dual-color calcium imaging technique that allowed us to simultaneously monitor these two neural ensembles while awake mice, of both sexes, passively viewed natural movies. SST neurons were more active during epochs of reliable pyramidal neuron firing, whereas PV neurons were more active during epochs of unreliable firing. SST neuron activity lagged that of PV neurons, consistent with a feedback inhibitory SST→PV circuit. To dissect the role of this circuit in pyramidal neuron activity, we used temporally limited optogenetic activation and inactivation of SST and PV interneurons during periods of reliable and unreliable pyramidal cell firing. Transient firing of SST neurons increased pyramidal neuron reliability by actively suppressing PV neurons, a proposal that was supported by a rate-based model of V1 neurons. These results identify a cooperative functional role for the SST→PV circuit in modulating the reliability of pyramidal neuron activity.

Key words: **inhibitory neurons; optogenetics; reliable processing; two-photon microscopy; visual cortex**

Significance Statement

Cortical neurons often respond to identical sensory stimuli with large variability. However, under certain conditions, the same neurons can also respond highly reliably. The circuit mechanisms that contribute to this modulation remain unknown. Here, we used novel dual-wavelength calcium imaging and temporally selective optical perturbation to identify an inhibitory neural circuit in visual cortex that can modulate the reliability of pyramidal neurons to naturalistic visual stimuli. Our results, supported by computational models, suggest that somatostatin interneurons increase pyramidal neuron reliability by suppressing parvalbumin interneurons via the inhibitory SST→PV circuit. These findings reveal a novel role of the SST→PV circuit in modulating the fidelity of neural coding critical for visual perception.

Received Dec. 18, 2020; revised Aug. 16, 2021; accepted Aug. 23, 2021.

Author contributions: R.V.R. and M.S. designed research; R.V.R., M.Y., M.H., and V.B.-P. performed research; R.V.R. and M.H. analyzed data; and R.V.R., M.Y., M.H., and M.S. wrote the paper.

R.V.R. was supported by the Howard Hughes Medical Institute International Student Research Fellowship. M.Y. was supported by the National Institute of Biomedical Imaging and Bioengineering Pathway to Independence Award K99EB027706. This work was supported by National Institutes of Health Grants EY007023, NS090473, and EY028219 and the Picower Institute Innovation Fund to M.S. The authors thank Sami El-Boustani and Sur lab members for discussions; Travis Emery and Liadan Gunter for technical assistance and animal husbandry; Rachel Neve for creating the FRT-GCaMP6f and FRT-ChR2 constructs; and the Genie Project at the Janelia Research Campus, Howard Hughes Medical Institute, for use of GCaMP6f and jRGECO1a.

The authors declare no competing financial interests.

Correspondence should be addressed to Mriganka Sur at msur@mit.edu.

https://doi.org/10.1523/JNEUROSCI.3176-20.2021

Introduction

A long-standing aim of systems neuroscience is to relate neural activity to perception. In visual perception, it has been established that a key role of the primary visual cortex (V1) is to transform raw sensory information from the environment into correlates of a low-level percept (Frégnac and Bathellier, 2015). Surprisingly, under laboratory conditions, V1 pyramidal neurons respond to repetitions of identical sensory stimuli with spike trains that vary greatly in both the number and the timing of spikes (Tolhurst et al., 1983; Softky and Koch, 1993). Although it is known that this unreliability limits stimulus selectivity (Kohn et al., 2016), the impact on perception, and more specifically, visually guided behavior, remains unknown. Notably, a large part of

Table 1. Summary of mouse genotypes and viruses used in each experiment

Figure	Mouse used	The Jackson Laboratory ID	Virus used
1	PV-Cre and SST-Cre x Ai14.	Stock #008069, https://www.jax.org/strain/008069 Stock #013044, https://www.jax.org/strain/013044 Stock #007908, https://www.jax.org/strain/007908	AAV1.Syn.GCaMP6f.WPRE.SV40
1	PV-Cre and SST-Cre	See above	AAV1.Syn.Flex.GCaMP6f.WPRE.SV40
2	PV-Flp x SST-Cre	Stock #022730, https://www.jax.org/strain/022730	AAV1.Syn.fDIO.GCaMP6f.WPRE.SV40 and AAV1.Syn.Flex.NES.jRGECO1a.WPRE.SV40 (1:2 mixture)
3	PV-Flp x SST-Cre	See above	AAV-CAG-Flex-ArchT-tdTomato and AAV1.Syn.fDIO.GCaMP6f.WPRE.SV40 (1:2 mixture)
3	PV-Flp x SST-Cre	See above	AAV1-EF1-dflox-hChR2(H134R)-mCherry.WPRE, AAV1.Syn.Flex.NES.jRGECO1a.WPRE.SV40, AAV1.Syn.fDIO.GCaMP6f.WPRE.SV40 (1:1:1 mixture)
4	PV-Cre x Ai32	Stock #012569, https://www.jax.org/strain/012569	AAV1.Syn.GCaMP6f.WPRE.SV40 and AAV2-CAG-FLEX-tdTomato (1:2 mixture)
4	PV-Flp x SST-Cre	See above	AAV1-EF1-fDIO-hChR2(H134R)-mCherry.WPRE AAV1.Syn.Flex.GCaMP6f.WPRE.SV40 (1:2 mixture)
6	SST-Cre x Ai32	See above	AAV1.Syn.GCaMP6f.WPRE.SV40 and AAV2-CAG-FLEX-tdTomato (1:2 mixture)
6	PV-Flp x SST-Cre	See above	AAV1-EF1-dflox-hChR2(H134R)-mCherry.WPRE, AAV1.Syn.fDIO.GCaMP6f.WPRE.SV40 (1:2 mixture)
9	PV-Cre x Ai35	Stock #012735, https://www.jax.org/strain/012735	AAV1.Syn.GCaMP6f.WPRE.SV40 and AAV2-CAG-FLEX-tdTomato (1:2 mixture)

the variability is generated internally within the cortex as the same neuron can respond either reliably or unreliably under different conditions (Azouz and Gray, 1999; Averbeck et al., 2006). For example, increasing the size of the stimulus within the receptive field (RF) or its statistics from simple (gratings) to complex (natural scenes) increases reliability (Rikhye and Sur, 2015). Additionally, arousal or attention decreases variability and increases task performance (Cohen and Maunsell, 2009; Reimer et al., 2014; Engel et al., 2016; Minces et al., 2017; Bondy et al., 2018). Collectively, these findings suggest that mechanisms might exist within the cortex to modulate response reliability depending on processing demands (Sprague et al., 2015; Liu et al., 2018). The goal of this study was to elucidate some of these mechanisms.

Inhibitory neurons (INs) play an important role in controlling cortical activity at various temporal and spatial scales (Isaacson and Scanziani, 2011). Hence, changes in cortical inhibition might be a potential mechanism responsible for modulating response reliability. It has been noted that inhibitory postsynaptic potentials measured in cortical pyramidal neurons are precisely delayed relative to excitatory potentials during epochs of reliable firing (Wehr and Zador, 2003). This delayed inhibitory input is believed to quench stochastic excitatory inputs by limiting integration to a small window during which reliable spiking can occur (Haider and McCormick, 2009). Moreover, chronically blocking inhibition sharply decreases response reliability (Egger et al., 2015; Zhu et al., 2015). However, given the computational diversity of INs, the specific role of different IN subtypes in modulating response reliability remains poorly understood (Tremblay et al., 2016; Wamsley and Fishell, 2017; Khan and Hofer, 2018; Ferguson and Cardin, 2020). This study focuses on the two main IN classes—parvalbumin-expressing INs (PV-INs) and somatostatin-expressing INs (SST-INs)—which provide distinct inhibitory control over pyramidal excitatory (EXC) neurons in layer 2/3 of mouse V1. PV-INs provide rapid, shunting inhibition onto the somatic compartment of EXC neurons (Rudy et al., 2011) and as a consequence are able to powerfully control the response gain (Atallah et al., 2012; Wilson et al., 2012; Liu et al., 2018) and spike timing (Pouille and Scanziani, 2001) of the PV-INs targets. SST-INs, on the other hand, inhibit the distal dendrites of pyramidal neurons, where they can control synaptic integration (Murayama et al., 2009; Lovett-Barron et al., 2012; Chiu et al., 2013; Yang et al., 2016). SST-INs also receive strong intracortical excitation and have been found to influence network integration (Adesnik et al., 2012; El-Boustani et al., 2014; Phillips and Hasenstaub, 2016). Importantly, these INs do not act independently as SST-INs also inhibit PV-INs (Cottam et al., 2013; Pfeffer et al., 2013; Tremblay et al., 2016). Through this inhibitory SST→PV circuit, SST-INs have the ability to control the inhibitory tone of both the dendritic and the somatic compartments (Yaeger et al., 2019), making them ideal candidates to modulate variability both at the level of synaptic input and spiking output. However, little evidence exists to support this hypothesis.

Here, we developed a line of double transgenic mice and used a multifaceted approach to study how interactions between PV- and SST-INs contribute to reliable sensory processing in V1. Using dual-wavelength calcium imaging, we found that SST-INs were more active during epochs of reliable pyramidal cell firing, whereas PV-INs were more active during epochs of unreliable firing. This complementary activity was because of the inhibitory SST→PV circuit. Using temporally limited optical perturbations, we found that SST-INs improve reliability by suppressing PV-INs. Thus, our work identifies a novel mechanism by which PV and SST-INs work cooperatively, via the SST→PV circuit, to modulate the fidelity of sensory processing.

Materials and Methods

Experimental animals. All experiments were conducted under protocols approved by the Massachusetts Institute of Technology Committee on Animal Care and conformed to National Institutes of Health (NIH) guidelines. The main mouse lines used in this study are provided in Table 1. All mice were maintained on a C57BL6/J background. Only mice older than 8 weeks, both male and female, were used in this study.

Mice were housed in the vivarium on a standard 12 h light/dark cycle with a maximum of five mice in each cage. Experiments were performed during the light portion of the cycle.

To create *SXP* mice, we crossed homozygous male SST-Cre mice with heterozygous female PV-Flp mice. Pups from the first offspring generation (F1) were genotyped at postnatal day 21 using a commercial service (Transnetyx), and only pups that expressed Cre and Flp were selected. Only F1 pups from three breeder lines were used in this study.

To create PV-ChR2, SST-ChR2, and PV-Arch mice, we crossed homozygous male PV-Cre or SST-Cre with heterozygous female Ai32 or Ai35 mice. Again, F1 pups were genotyped at postnatal day 21 using a commercial service (Transnetyx), and only pups that expressed Cre and GFP, the fluorophore attached to channelrhodopsin-2 (ChR2; or EYFP in the case of Ai35 mice) were selected. Only F1 pups from six breeder lines were used in this study.

Surgical procedures. Adult mice (between 8 and 10 weeks old) were anesthetized with 1–2% isoflurane (v/v), and a sterile surgery was performed as described previously (Rikhye and Sur, 2015; Goard et al., 2016). First, a small circular piece of scalp was excised to expose the skull. After cleaning and drying the skull using a razor blade and sterile cotton swabs, a custom-built head post was implanted in the exposed skull with cyanoacrylate glue (Loctite) and cemented with dental acrylic mixed with black paint (C&B-Metabond). A craniotomy (3 mm in diameter) was made over the left V1 (2.5 mm lateral and 0.5 mm anterior to λ). Care was taken not to damage the dura during the craniotomy.

Depending on the experiment, a cocktail of adeno-associated viruses (AAVs; Table 1) were then injected using a beveled pipette (20–30 μm diameter tip, Drummond Scientific) backfilled with mineral oil at a speed of 50 nl/min at five to six injections sites. Between 100 and 150 nl of virus was injected per injection site. After each injection, pipettes were left in the brain for an additional 5–10 min (depending on injection volume) to prevent backflow and to ensure proper virus spread. Following virus injections, a chronic imaging window was placed in the craniotomy. The imaging window consisted of an inner 3 mm glass window and an outer 5 mm glass window (Warner Instruments), which were glued together using optically transparent UV curing glue (Norland Optical). Once mice recovered from anesthesia, they were returned to their home cage and were singly housed. Mice were provided with analgesia (meloxicam, 0.1 mg per kg of body weight) subcutaneously 3 d postsurgery. Imaging experiments typically started 14–21 d postsurgery to allow for sufficient viral expression and recovery. Mice with limited optical access because of bone growth or infection were excluded from further analysis.

Two-photon imaging. Imaging was performed using a Prairie Ultima two-photon system (Bruker) driven by two Spectra Physics Mai Tai lasers, both passed through DeepSee modules (Spectra Physics). Imaging was performed using a high-performance objective lens (Olympus XL 25× Plan N objective, numerical aperture = 1.05). In most experiments (except dual-wavelength imaging; see below), we tuned the laser to 965 nm to enable us to optimally visualize both GCaMP6f and tdTomato fluorescence. To separate red and green fluorescence (Meng et al., 2018), we used a 570 nm dichroic filter, a 520/50 nm green filter, and a 620/90 nm red filter (Chroma). We used a removable curtain made from blackout material (Thorlabs) and a custom holder to isolate the visual display from the microscope.

In dual-wavelength imaging experiments, we tuned one laser to 920 nm to excite GCaMP6f and another laser to 1020 nm (the limit of the laser) to excite jRGECO1a. Both laser beams were multiplexed using a half-wave plate and a polarizing beam splitter (Thorlabs) before being focused onto a pair of galvanometer mirrors. In doing so, mirrors scanned both laser beams over the same neural field of view (FOV). This allowed us to image from jRGeco1a-expressing SST and GCaMP6f-expressing PV neurons within the same neural population simultaneously.

In all experiments, images were acquired using ScanImage r3.8 in MATLAB (Vidrio Technologies) at 20 Hz, 512 × 100 pixels (2× optical zoom). The images covered a cortical area of ~150 μm × 150 μm. Images were collected at a depth of 180–280 μm below the pial surface, which corresponds to cortical layer 2/3. Before imaging, mice were habituated to head fixation for 2–3 sessions to reduce stress and anxiety. Typically, 5–8 nonoverlapping FOVs (each an independent neural population) were collected for each mouse. FOVs were determined by hand mapping the receptive field locations of neurons in the FOV by moving a sinusoidal grating within a 20° Gabor patch around the screen in 20 × 20° square patches. FOVs without visually evoked responses to these stimuli or those with receptive fields close to the edges of the monitor were discarded.

Visual stimuli. Natural movies from the Van Hateren database, as previously described (Rikhye and Sur, 2015), were displayed on a γ corrected, 7 inch 1080 p LCD computer monitor (Xenarc) placed 3 inches in front of the contralateral eye. All movies were in grayscale. This computer monitor covered a visual space of ~50 × 70°. Stimulus timing was controlled using Psychtoolbox-3 with custom written MATLAB (MathWorks) scripts. Each movie was presented for 4 s (30 frames/s) and stimuli were interleaved with a 4 s isoluminant gray screen. Each movie frame was adjusted to have a luminance of 128 (mean of pixel histogram) and an root mean squared (RMS) contrast of 32 (RMS of pixel histogram) on a 0–255 grayscale using the SHINE toolbox(Willenbockel et al., 2010).

Optical activation and inactivation. A 473 nm (blue, 200 mW peak power) laser and a 532 nm laser (300 mW peak power, Opto Engine) were used to activate ChR2 and Arch respectively. Both lasers were coupled to a 0.12 NA optical fiber (Thorlabs), and these fibers were launched into the uncaging beam path of the two-photon microscope. The uncaging beam path was coaligned with the imaging path so that the single wavelength laser illuminated the same FOV as the two-photon laser. In this way, we were able to provide focused activation (or inactivation) of neurons within the same FOV. These single wavelength lasers were triggered using a transistor-transistor logic (TTL) pulse generated by the visual stimulus computer (see description below). Laser power at the tip of the objective was 1.5 mW for ChR2 and 2.5 mW for Arch experiments, respectively. Laser power was measured (catalog #S145C, Thorlabs) before the start of each experiment. Using single-cell imaging, we determined that these laser powers were sufficient to reliably drive activation (or suppression) of PV-INs and SST-INs neurons (see Fig. 6*A–D*). These power values are also consistent with previously published reports using similar mice (Madisen et al., 2012; Seybold et al., 2015).

In all experiments, we used a stimulus-triggered random stimulation protocol to activate/inactivate cells (see Fig. 4*A*). In ChR2 experiments, each stimulation pattern consisted of four 20 ms pulses of laser with a 10 ms interpulse interval (i.e., 110 ms total duration per stimulation epoch). In Arch experiments, we used 2 × 40 ms laser pulses with a 5 ms interpulse interval (175 ms total duration). This pulse pattern was applied at 22 different frames during a natural movie. The frame numbers that triggered the pulses were fixed for each experiment. Specifically, the first pulse occurred at stimulus onset (i.e., triggered by frame number 1), the last pulse occurred at stimulus offset (frame number 240), and the remaining 20 pulses were chosen at a fixed interval. Before the start of each experiment the order of these pulses was pseudorandomized; the order was noted and used for *post hoc* analysis (described below). This was done to minimize spurious network activity caused by rhythmic photostimulation. To calculate reliability, each pulse pattern was repeated 10 times. This resulted in a total of 220 Laser-on events and 10 Laser-off events (used for controls). Also, to prevent adaptation to repeated presentations of one movie, we interleaved the pulsed movie with a nonpulsed movie, during which no laser was applied. As a consequence, the network was allowed at least 8 s to recover before the next laser pulse was applied.

To determine which two movies to select, we first presented 40 repetitions of five different movies and computed reliability of each neuron in that FOV as described below. Movies with the highest two reliability values were then selected as the pulsed and nonpulsed movie. This method was repeated systematically for each FOV and helped us reduce the number of unreliable or nonvisually responsive neurons.

Visually responsive neurons and spike rate inference. All data analysis was performed with custom-written MATLAB (MathWorks) and ImageJ (NIH) macros that called on built-in functions. Following imaging, images stacks (TIFF format) were first corrected for motion artifacts

using an open-sourced ImageJ plug-in (https://sites.google.com/site/qingzongtseng/template-matching-ij-plugin), which maximized the cross-correlation coefficient between frames. Frames with excessive motion artifacts that could not be corrected were discarded. Frames with photostimulation laser artifacts were also discarded from analysis (usually one to two frames), and cubic spline interpolation was used to smooth over these blanked frames.

Next, neuronal regions of interest (ROIs) were manually segmented in ImageJ (NIH) using the Cell Magic Wand tool (https://www.maxplanckflorida.org/fitzpatricklab/software/cellMagicWand/), and fluorescence time series for each neuron was computed by averaging pixels within each ROI. A modified version of the Cell Magic Wand tool was used to identify a surrounding neuropil region, which was an annulus of outer diameter = (15 pixels + diameter of cell) around each cell. These data were then imported into MATLAB for further analysis. The raw fluorescence of each cell was computed using the following formula: $F = F_{Raw} - F_{neuropil}$ (Kerlin et al., 2010; Siegle et al., 2021).

All data analysis was performed using custom-written scripts in MATLAB. Significantly visually responsive cells were determined from the fluorescence time changes (ΔF/F) by performing a one-tailed Student's *t* test between visually evoked (4 s movie on) and spontaneous responses (4 s gray screen in between movies). To obtain a better estimate of the spontaneous activity we also collected 120 s of activity to an isoluminance gray screen before the start of each experiment. Only cells with $p < 0.001$ were classified as visually responsive.

We used a two-step procedure to estimate the firing rates of visually responsive cells. We first detected statistically significant calcium transients from the ΔF/F time series of each neuron by analyzing the distribution of positive-going and negative-going calcium transients as described previously (Dombeck et al., 2007; Danielson et al., 2016). This method allowed us to minimize the number of false-positive calcium transients induced by brain motion (false-positive error rate <1%). Next, we filtered the ΔF/F time series of each neuron so that nonsignificant transients were zero, and significant transients were untouched. Following this, we used an optimized deconvolution algorithm for GCaMP6f (Theis et al., 2016; Sebastian et al., 2019) to infer the firing rate for each neuron. Briefly, this algorithm inferred the probability of spiking from statistically significant calcium transients. To convert this probability into a firing rate (measured in events/s), we multiplied each probability by 20 Hz, the frequency at which the calcium transients were sampled. Unless otherwise stated, all data analysis was performed using inferred firing rates.

Change in firing rate and change in reliability following photostimulation. In all photostimulation experiments, analysis was restricted to a 600 ms time window (12 imaging frames) following laser activation. Within this time window, we determined the change in firing rate using the following formula:

$$\Delta Rate(p) = \frac{Rate_{Laser\,on}(p) - Rate_{Laser\,off}(p)}{Rate_{Laser\,off}(p)},$$

where *p* is the pulse number. Because each neuron responded at different time points of the movie, averaging this across the population of neurons would obscure any changes in the firing rate (or reliability). Thus, we aligned the firing rate trace of each neuron obtained on the Laser-off trials (control condition) so that the maximum rate occurred at 1 s following stimulus onset. This time index was then used to align the firing rate traces on the Laser-on trials.

Response reliability to natural movies was calculated using the following equation:

$$\text{Reliability} = \frac{2}{T^2 - T}\sum_{i=1}^{T}\sum_{j=i+1}^{T}\frac{f_{i,A} - \widehat{f_{i,A}}, f_{j,A} - \widehat{f_{j,A}}}{f_{i,A} - \widehat{f_{i,A}} f_{j,A} - \widehat{f_{j,A}}},$$

where $i, j \in [1, T]$ are the index trial numbers and $f_{i,A}$ is the rate on the ith trial for movie A, $\widehat{f_{i,A}}$ is the average rate for that trial, and $\widehat{f_A}$ is the average across trials (mean rate). Thus, from this equation the response reliability is the average correlation of all pairwise combinations of trials, corrected for differences in mean firing rate (Rikhye and Sur, 2015). Similarly, we computed an unbiased estimate of the firing rate variance between trials for movie A using the following formula:

$$\text{Variance} = \frac{1}{T-1}\sum_{i=1}^{T}\left(f_{i,A} - \widehat{f_A}\right)^2.$$

In photostimulation experiments, the change in reliability induced by laser activation was calculated using the following formula:

$$\Delta Reliability(p) = \frac{Rel_{Laser\,On}(p) - Rel_{Laser\,off}(p)}{Rel_{Laser\,off}(p)}.$$

Similar to the firing rate, we aligned the reliability on the Laser-off trials so that each neuron was maximally reliable at 1 s. The same time index was then used to align reliability on the Laser-on trials. To determine the epoch of maximum and minimum reliability, we calculated the time index corresponding to the maximum and minimum reliability on the Laser-off trials from unaligned traces. For the regression analysis (see Figs. 3, 4, 6), we computed the change in variance using the simple formula as follows:

$$\Delta Var(p_{max,min}) = Var_{Laser\,On}(p_{max,min}) - Var_{Laser\,Off}(p_{max,min}).$$

A similar formula was used to calculate Δ*Rate* and Δ*Reliability*.

Multiunit rate-based neural network model. We built a simple four-unit rate-based model of layer 2/3 of visual cortex to study, as proof of concept, the effects that the SST-PV dynamics had on EXC neuron reliability. Each population was represented by the following single rate-based equation:

$$\tau_x\frac{dr_x}{dt} = -r_x + f\left(\sum_y W_{xy}r_y + I_x^{vis\,input} + I_x^{bg\,input} + I_x^{Opto}\right),$$

where r_x is the firing rate of the cell population x (EXC, PV, SST, VIP). PV units had a time constant $\tau_x = 10ms$, whereas EXC, SST, and VIP units had a slower time constant $\tau_x = 20ms$ (Kuchibhotla et al., 2017). We modeled the rate-current transfer function of each population using the power-law function as follows:

$$f(I) = 0.01(I_+)^{2.2}.$$

EXC, PV, and SST units received visual input ($I_x^{vis\,input}$), which accurately reflected the temporal activity of natural movie stimulation (Fig. 7*A–C*). This visual input was the summed activity of a bank of 50 linear-nonlinear-Poisson (LNP) units. The linear filter consisted of a spatial log-Gabor receptive field [total of six different orientations (0–180°) and ranged in size from 12 to 18° of visual angle] and γ functions with a range of temporal delays (140–200 ms). These spatiotemporal receptive fields closely resemble those seen in mouse visual cortex (Bonin et al., 2011; Rikhye and Sur, 2015). Because we did not know the locations of the receptive fields (RFs) a priori, we randomly picked 50 possible locations on the screen. The same natural movies used in our experiments were first convolved with each spatiotemporal log-Gabor filter, which was then rectified with a pointwise nonlinearity to produce a firing rate estimate. This firing rate estimate was then used to generate an inhomogeneous Poisson spike train. To generate input to the different units in the model, we filtered this Poisson spike train through a facilitating α synapse to generate the current $I_x^{vis\,input}$. The weight of each synapse was varied from trial to trial, which together with the stochastic nature of the Poisson process, created trial-to-trial variability in the model, which closely resembled the variability observed between movies (see Fig. 7*D*). EXC and PV units received summed input from units with smaller log-Gabor sizes, whereas SST units received input from larger log-Gabor

sizes reflecting differences in preferred spatial frequencies of each cell type (Ma et al., 2010). VIP units did not receive any visual input.

All units received background current ($I_x^{bg\ input}$), which was modeled as a stochastic Poisson process. We varied input rates between the different units (EXC and SST = 10 Hz, PV = 24Hz, VIP =15 Hz) to match spontaneous firing rates observed *in vivo*. In this way, the spontaneous activity was uncorrelated between each neuronal subtype in our model and therefore represented an independent source of noise.

In experiments with optogenetic perturbation, we modeled optogenetic input into both PV and SST units (I_x^{Opto}) as a train of square wave pulses, which mimicked the temporal properties of the laser stimulation used in our experiments. To test for robustness and to mimic natural trial-to-trial variability of ChR2 and Arch, we varied the pulse amplitude by ± 10% in each trial by drawing values from a uniform distribution. The amplitude values were SST-ChR2 = 25 mA, PV-ChR2 = 45 mA, and PV-Arch = −50 mA.

Connections among populations were given via the following weight matrix:

$$W = \begin{bmatrix} Wee & Wep & Wes \\ Wpe & Wpp & Wps \\ Wse & Wsp & Wss \end{bmatrix} = \begin{bmatrix} 0.817 & -0.986 & -0.412 \\ 0.8535 & -0.99 & -0.387 \\ 0.878 & 0 & 0 \end{bmatrix},$$

where W_{xy} is the weight of the connection from neuron y to neuron x. In some experiments, we parametrically reduced the strength of the SST→PV connection by setting W_{PS} to either 75, 50, 25, or 0% of the original value. This weight matrix reflects the known connectivity between neuron subtypes in the visual cortex and is derived from previously published results (Pfeffer et al., 2013; Litwin-Kumar et al., 2016). These connection weights were adjusted so that the model responses and reliability matched our experimental observations (see Fig. 8*D*).

To compute reliability, we simulated 30 trials with the same visual stimulus, and used the same equation above to compute EXC unit reliability. To test the robustness of our model to parameter changes, we created 500 models (see Fig. 8, each dot) by independently varying all the parameters of the model by ± 10% of the current values. Numerical integration was performed in MATLAB using the forward Euler method with a time step of 0.05 ms.

To determine which factors (e.g., PV suppression, EXC suppression) contributed the most to the changes in EXC unit reliability following PV/SST activation/suppression, we performed multivariate linear regression using the following model:

$$\Delta EXC Reliability \sim \beta_0 + \beta_1 \Delta SST\ Firing\ Rate + \beta_2 \Delta PV\ Firing\ Rate + \beta_3 \Delta EXC\ Firing\ Rate + \beta_4 \mathrm{EXC\ reliability\ (pre)}.$$

Linear regression was performed in MATLAB (using the fitlm function), and statistical tests (Student's *t*) were computed to assess the significance of each predictor.

Experimental design and statistical analysis. All statistical analyses were performed using custom-written scripts in MATLAB and R. No tests were conducted to determine sample size. Data were first tested for normality using the Shapiro–Wilk test. All data presented here are non-normally distributed, thus all statistical tests were conducted using nonparametric statistics. Although no additional tests were performed to determine sample sizes, the number of animals used in each experiment is comparable to that of similar studies in the field (Rikhye and Sur, 2015; Zhu et al., 2015). Information about the number of mice and sex is provided in the figure legends.

Our experiments involved testing the influence of laser activation on the same population of neurons; thus all comparisons were performed using nonparametric repeated-measures ANOVA (Friedman test) with Bonferroni's correction, and rank-sum *post hoc* tests with significance value was set to 0.05. *Post hoc* tests were performed using the two-tailed Wilcoxon rank-sum test relative to the Laser-off condition. To determine whether the change in reliability was significant, we performed permutation tests (corrected for familywise error rate) where we resampled with replacement (10,000 permutations) from the change distribution and tested whether the sampled distribution was significantly different from zero using a one-tailed rank-sum test. Unless otherwise stated, data are presented as median ± 95% CI (calculated using bootstrap sampling). All confidence intervals were determined using bootstrap. All box-whisker plots show median (notch), interquartile range (box edges), and data range (whiskers). All *p* values are labeled in the figures and in the corresponding legends.

Data availability. All scripts used in analysis and model simulations are available on Github (https://github.com/toxine4610/PV_SST_Circuits). Raw imaging and other data are available from the corresponding author on reasonable request.

Results

SST and PV-INs have mutually exclusive dynamics during epochs of reliable firing

To simultaneously image inhibitory and pyramidal neurons in layer 2/3 of V1, we expressed the genetically encoded calcium indicator (GECI) GCaMP6f in PV-tdTomato and SST-tdTomato mice (PV-Cre and SST-Cre x Ai14) via stereotactic injections of an adeno-associated virus (Fig. 1*A*; see above, Materials and Methods). Because PV- and SST-INs in these mice expressed the red fluorescent protein, tdTomato (see above, Materials and Methods, our optical setup to minimize spectral overlap between red and green channels), we reasoned that the majority of tdTomato-negative neurons would primarily be pyramidal EXC neurons. We measured the reliability of EXC neurons in awake, passively viewing mice to repeated presentations of naturalistic movies (five different movies) using two-photon calcium imaging. We used natural movies because they are known to drive sparse and reliable responses from EXC neurons across different species (Kayser et al., 2003; Haider et al., 2010; Froudarakis et al., 2014; Rikhye and Sur, 2015). We quantified the trial-to-trial response reliability of these EXC neurons for each movie by computing the average of all pairwise correlations (corrected for differences in the mean firing rate) between single trial responses (see above, Materials and Methods). By this definition, reliability measures the degree of trial-to-trial similarity in evoked responses to a given movie. As expected, response reliability was strongly negatively correlated with between-trial variability (Fig. 1*B*,*C*), as the least variable neurons also had responses that were highly similar across trials.

In all imaged populations (10 mice, 1101 neurons), EXC activity patterns spanned a range from highly stereotyped and reliable responses to weak and variable activity. On average, however, most neurons (37.7 ± 15.4%) in each population responded reliably (>0.4; i.e., similar responses on at least 40% of the trials) to at least one movie. EXC neuron activity was typically punctuated by brief epochs of highly reliable responses (Fig. 1*B*). These observations agree with previous studies (Froudarakis et al., 2014; Rikhye and Sur, 2015), and establish that naturalistic movies can drive EXC neurons in mouse V1 to respond reliably and with low variability between trials.

We found there was a strong correlation between reliability values computed directly from the changes in fluorescence values compared with those computed from spike rates inferred from the calcium traces (Fig. 1*D*). This suggests that applying additional processing to the calcium signal in the form of deconvolution does not change the interpretation of trial-to-trial reliability. Importantly, deconvolution helps to remove the long tails of calcium indicator fluorescence decay (Pnevmatikakis et al., 2016; Sebastian et al., 2017, 2019; Stringer and Pachitariu, 2019; Wei et al., 2020), which in turn would result in artificially higher reliability values. These data indicate that the deconvolution

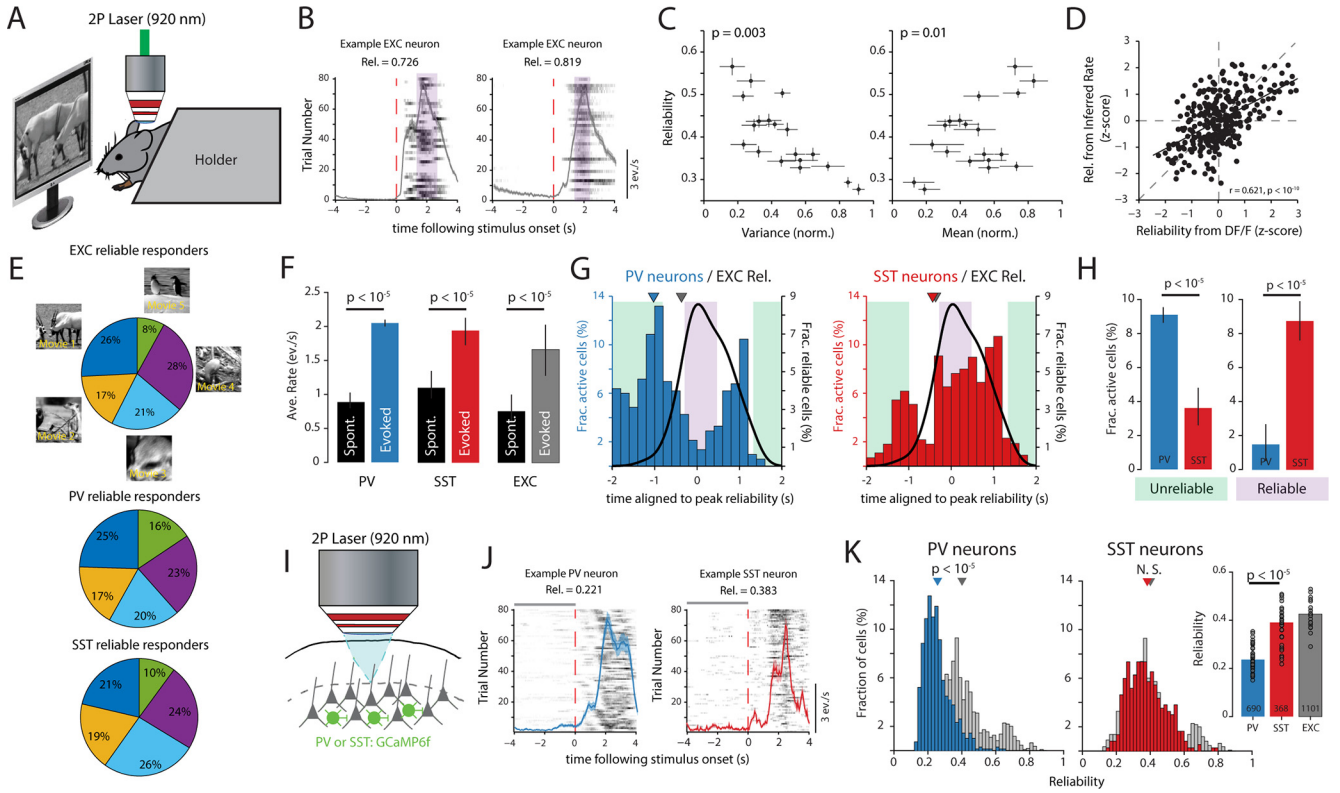

Figure 1. SST and PV-INs respond during distinct epochs of EXC neuron activity. ***A***, Schematic showing experimental setup and method to record from EXC neurons. ***B***, Raster plots (trials vs time) of two simultaneously recorded EXC neurons showing reliable and sparse responses to the same movie. Gray lines show trial-averaged responses, and shaded areas indicate SEM over trials. Shaded purple bar shows time period (epoch) when these EXC neurons are reliably activated. ***C***, Scatter plot showing strong negative (positive) correlation between intertrial variance (mean) and response reliability. Each data point is the mean response reliability and the across-trial variance of each imaged population, error bars indicate SEM (19, each with 22–87 neurons; 10 mice, 6 female, 4 male). ***D***, Scatter plot showing the correlation between reliability computed from either DF/F or inferred spike rates. ***E***, Pie charts showing moviewise distribution of reliably responding EXC (top), PV (middle), and SST (bottom) neurons. Movies that recruit a greater fraction of reliably responding EXC neurons also recruit more reliably responding PV and SST-INs. ***F***, Comparison between evoked (averaged from 5 different movies) and spontaneous (Spont., gray screen) activity for all the three cell types, expressed in number of inferred events per second. All cell types showed a significant increase in evoked response rate compared with spontaneous activity. Error bars indicate SEM. ***G***, Histogram showing the fraction of active PV (left) and SST-INs (right) in 200 ms time bins aligned to peak EXC population reliability. Triangles above the histograms indicate mean time to peak activity. There was a significant difference between PV and EXC neuron activation times ($p < 10^{-6}$) but no significant difference between activation times for SST and EXC neurons ($p = 0.129$). Data in ***G*** are from 10 mice (sex as mentioned above; 1101 EXC neurons, 120 SST-INs, 186 PV-INs). ***H***, Bar plots comparing the median fraction of active PV and SST-INs during epoch of unreliable and reliable EXC neuron firing, respectively. Error bars indicate 95% CI. ***I***, Method to image INs. ***J***, Example raster plot of a PV and an SST-IN to the same movie. Format same as ***B***, ***K***, Histogram of PV and SST-IN reliability in relation to EXC neuron reliability (gray). Triangles above the histograms indicate mean reliability pooled over all neurons. Inset, Comparison of median reliability for all cell types. Each data point is the median reliability of each imaged population. Data from PV = 8 mice (690 neurons; 5 male, 3 female); SST = 8 mice (368 neurons); EXC = 10 mice (1101 neurons). All p values computed using grouped Bonferroni-corrected rank-sum test. N.S., non-significant.

faithfully captures the spike rates of cortical neurons (Vogelstein et al., 2010; Kwan and Dan, 2012; Berens et al., 2018; Evans et al., 2019; Ali and Kwan, 2020; Wei et al., 2020; Lawrence et al., 2021).

With the aim of elucidating the inhibitory mechanisms responsible for this reliable coding of naturalistic scenes (Fig. 1*E*), we first quantified the response properties of different IN subtypes to the same movies. Similar to EXC neurons, both PV-INs and SST-INs responded to these movies with an approximate twofold increase in response rate over spontaneous activity (Fig. 1*F*). Notably, there was no significant difference in evoked response rates between these INs ($p = 0.131$, rank-sum test). Interestingly, we noticed that movies that recruit a greater fraction of reliably responding EXC neurons also recruit more reliably responding PV-INs and SST-INs (Fig. 1*E*).

To further examine the relationship between EXC reliability and IN activity, we characterized PV-IN and SST-IN activity around epochs of reliable/unreliable EXC neuron firing. In each simultaneously recorded neural population, we computed the reliability of EXC neurons and the mean rate of P-INs/SST-INs in 200 ms time bins following stimulus onset. In each time bin, we then computed the fraction of reliably responding EXC neurons (i.e., neurons with reliability >0.4), which gave us a measure of how consistently the population responded to each movie repetition and the fraction of active PV-INs/SST-INs. Aligning the fraction of active INs to the epoch of maximum reliability, which facilitated comparisons between different movies and populations so that each had different response dynamics, revealed that the majority of PV-INs were active during epochs of unreliable EXC neuron firing (Fig. 1*G*,*H*). In contrast, SST-INs were most active during epochs when EXC neurons were most reliable. Therefore, although similar in response magnitude, PV-INs and SST-INs are active during distinct epochs of EXC neuron activity.

Do INs also respond reliably to these movies? To better quantify the reliability of the different IN subtypes, we restricted GECI expression to INs by injecting an adeno-associated virus encoding a Cre-dependent variant of GCaMP6f in either PV-Cre or SST-Cre mice (Fig. 1*I*). This method allowed us to avoid neuropil contamination from neighboring EXC

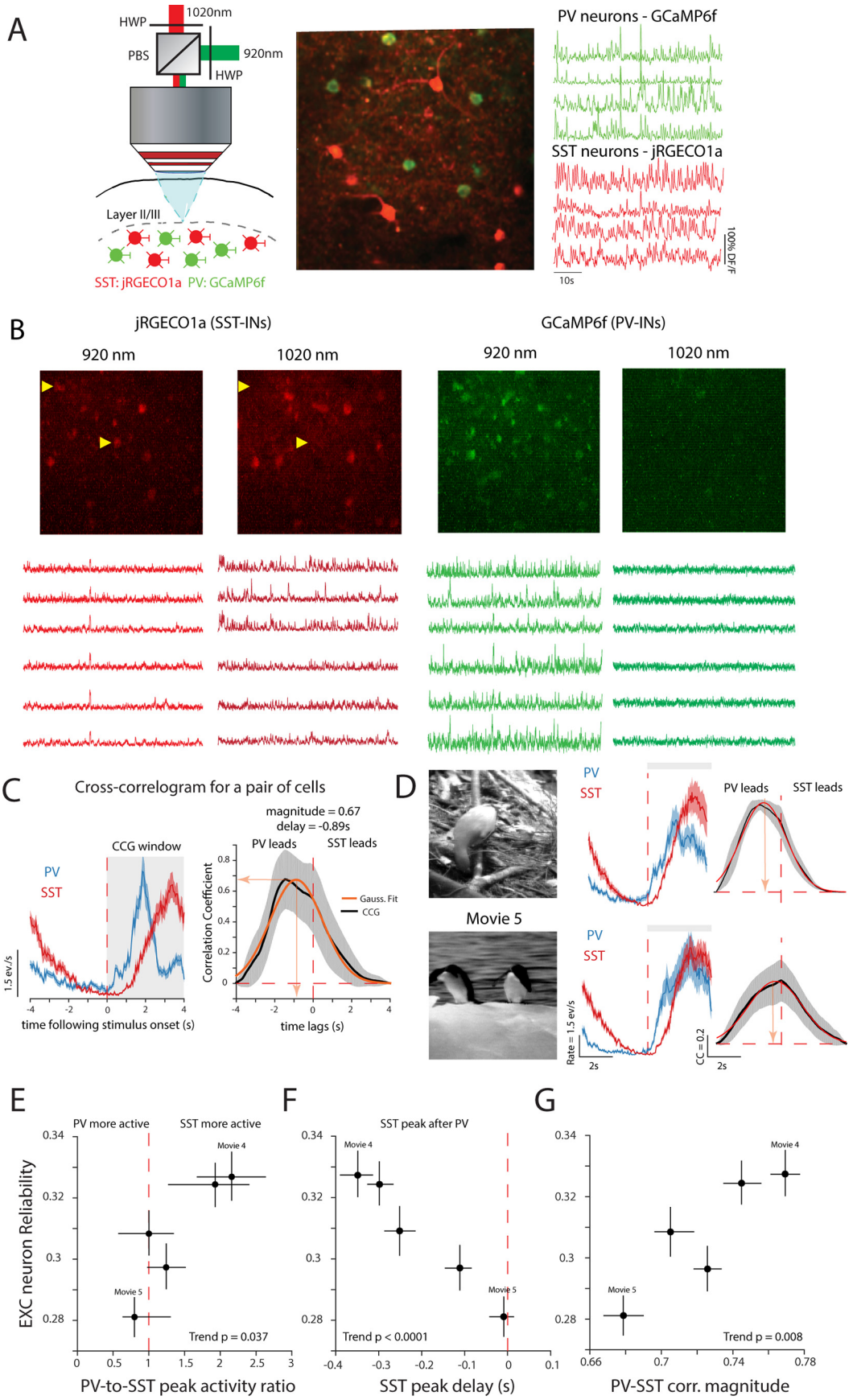

Figure 2. SST-INs are temporally delayed relative to PV-INs in reliably processed movies. ***A***, Left, Experimental setup. Briefly, a 1020 nm laser and a 920 nm laser were combined using a half-wave plate (HWP) and a polarizing beam splitter (PBS) to optimally activate jRGECO1a and GCaMP6f in SST and PV-INs, respectively (see above, Materials and Methods). Middle, Example field of view showing colabeled PV and SST-INs. Image covers a cortical area of 150 μm × 150 μm. Right, Example calcium transients from simultaneously recorded interneurons. ***B***, Top,

neurons. Interestingly, although PV-INs responded strongly to most movies, the responses were much more variable between trials (Fig. 1*J*,*K*). As a consequence, PV-INs were less reliable than EXC neurons. In contrast, SST and EXC neurons had similar reliability values (Fig. 1*J*,*K*).

Together, these results suggest two complementary modes of inhibition, with SST-INs providing reliable inhibition during epochs of reliable EXC firing and PV-INs providing unreliable inhibition during unreliable epochs.

The joint dynamics of SST and PV-INs scale with EXC reliability

Given this complementary relationship between PV and SST-INs, we next sought to characterize the trial-by-trial interactions between PV and SST-INs within the same neuronal population. To gain independent genetic access to both cell types (He et al., 2016), we crossed SST-Cre mice with PV-FlpO mice to create a strain of double transgenic mice (SXP mice), where SST-INs express *Cre* recombinase and PV-INs express *flp* recombinase. To monitor the joint activity of these IN subtypes *in vivo*, we concurrently expressed the red GECI (jRGECO1a) in SST-INs and the green GECI (GCaMP6f) in PV-INs in SXP mice and performed dual-wavelength calcium imaging (Fig. 2*A*). Using custom optics and filters, we scanned the same field of view with two multiplexed lasers, one tuned to 1020 nm to excite jRGECO1a and the other tuned to 920 nm to excite GCaMP6f (see above, Materials and Methods). These wavelengths optimally excite each GECI with very little spectral overlap (Dana et al., 2016; Fig. 2*B*). Notably, we observed a negligible fraction of colabeled cells (data not shown), confirming that the labeled PV-INs and SST-INs were indeed nonoverlapping cell types (Tremblay et al., 2016).

To quantify the temporal relationship between these INs we first computed CCGs between single trial responses of PV and SST-INs. We then estimated the activation delay and the correlation strength between each pair from the Gaussian function that best fit the CCG (average fit $R^2 = 78.9 \pm 4.6\%$; Fig. 2*C*). Across all recorded pairs, we measured an average time lag of −321 ms (CI, −360 to −283 ms), indicating that most SST-INs respond after PV-INs (75.44% of pairs, five mice; Fig. 2*C*). Note that this delay measures the time difference between the peak calcium activity of SST and PV-INs, and not the spiking onset latency, which is significantly shorter (Ma et al., 2010).

Interestingly, the strength and timing of these interactions also differed between movies, with some movies evoking more temporally correlated and delayed activity than others (Fig. 2*D*). Given that EXC neuron reliability also varied between movies, we next sought relate joint PV-SST activity with EXC reliability. However, because of technical limitations, we were unable to record from all three cell types simultaneously. Thus, we compared simultaneously recorded joint PV-SST activity to EXC neuron reliability obtained from separate mice but using the same movies and at similar cortical locations (Fig. 1, data). Movies that were more reliably processed (i.e., those with higher median EXC neuron reliability) evoked stronger activity from SST than PV-INs (Fig. 2*E*), which was consistent with our data in Figure 1. Furthermore, PV-SST pairs were more strongly correlated and had longer delays in movies that were more reliably processed, than movies that were less reliably processed (Fig. 2*E*–*G*). Multivariate linear regression analysis confirmed that the ratio of

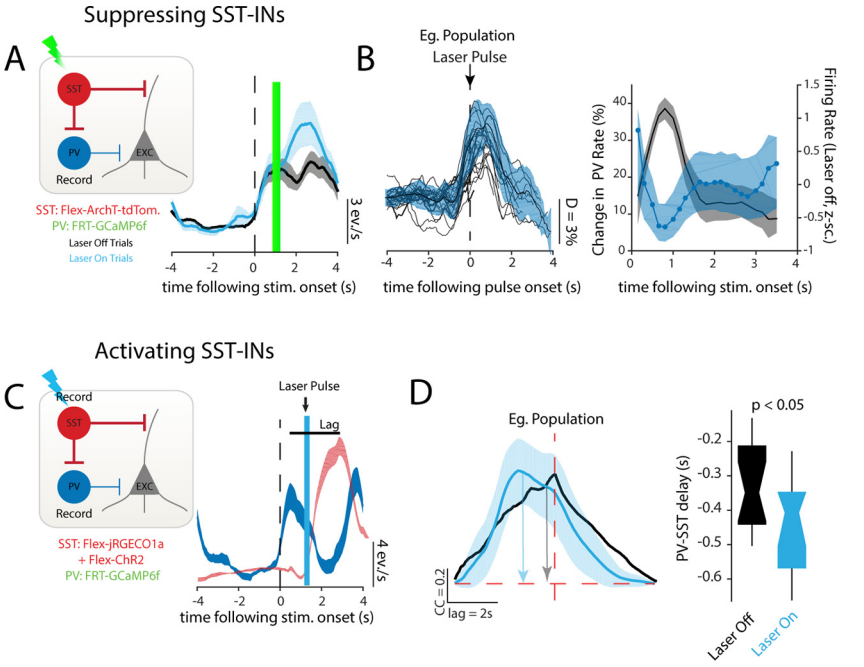

Figure 3. SST-INs strongly inhibit PV-INs via the SST→PV circuit. ***A***, Inset, Cre-dependent ArchT was expressed in SST-INs, and Flp-dependent GCaMP6f was expressed in PV-INs in SXP mice. Representative trial-averaged firing rate from one PV-IN showing that suppressing SST-INs strongly increases the firing rate of PV-INs. Shaded area indicates SEM over trials. ***B***, Left, Response rate change in one representative population of PV-INs (8 neurons) aligned to laser onset. All PV-INs increase firing rates following suppression of SST-INs. Right, Quantification of change in response rate of PV neurons following SST suppression relative to response rate on Laser-off trials. There is a significant increase in PV activity ($p < 0.001$, permutation test) regardless of when SST-INs are suppressed during a movie. Shaded area, 95% CI. Data from three mice (121 PV neurons). ***C***, Inset, Cre-dependent ChR2 and jRGECO1a were expressed in SST-INs, whereas Flp-dependent GCaMP6f was expressed in PV-INs in SXP mice. Representative example trial-averaged firing rate from one simultaneously imaged PV-SST pair, showing a strong suppression of PV-INs following SST-IN activation. The peak suppression occurs almost at the same time as SST-INs reach peak activation. ***D***, Left, Example cross-correlogram between all pairs of simultaneously recorded SST ($n = 4$) and PV-INs ($n = 9$) for an example population, showing the effect of SST activation on the time lag between PV and SST-INs. Gaussian fit is not shown. Data here are averaged over all stimulation epochs. Shaded area indicates SEM. Right, Box-whisker plot showing that activating SST-INs increases the time lag between PV and SST-INs ($p = 0.235$, Bonferroni-corrected rank-sum test). Data from three mice (84 PV neurons, 39 SST neurons), all males.

←

Images of jRGECO1a-expressing SST-INs and GCaMP6f-expressing PV-INs taken at 920 nm and 1020 nm, respectively. Bleed through from the green to the red channel can be clearly seen at 920 nm (yellow arrowheads). In contrast, no green signal can be detected at 1020 nm. Bottom, No jRGECO1a activity can be detected at 920 nm compared with 1020 nm. In contrast, no GCaMP6f activity can be detected at 1020 nm. Each trace is matched to the same neuron and shows activity in response to a series of natural movies (800 s long, acquired at 20 Hz). ***C***, Left, Trial-averaged responses from a pair of simultaneously recorded PV and SST-INs. Right, CCG of this pair. Orange line shows Gaussian fit to trial-averaged CCG. Shaded areas indicate SEM over trials. ***D***, Difference in correlation for two different movies for the same PV and SST-IN pair. ***E–G***, More reliable movies have a stronger SST peak activity compared with that of PV. ***E***, Longer delays between SST and PV peak activity (***F***) and stronger PV-SST correlation at peak delay (***G***). Data are from 2292 pairs, 5 mice (3 female, 2 male). Data points denote median ± 95% CI for each movie; *p* values computed using *F* test to measure significance of the trend relative to a constant model.

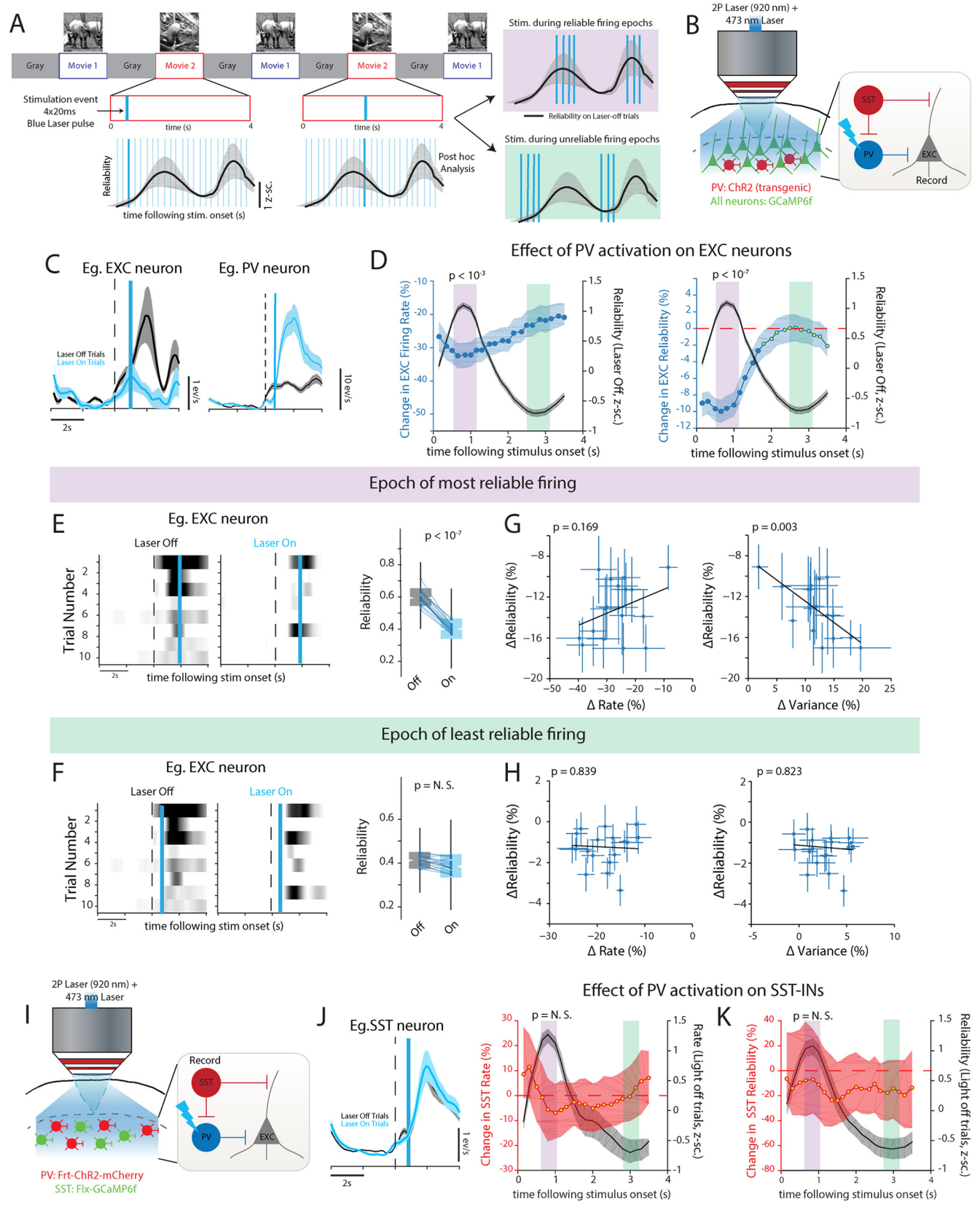

Figure 4. Increasing PV-IN activity reduces EXC neuron reliability. ***A***, Diagram describing random stimulation strategy. A brief laser pulse (stimulation event) was applied at 22 equally spaced time points during a 4 s movie (light blue lines). At each movie repetition, stimulation event time is drawn from this distribution at random (dark blue line). The bottom plots show the timing of each stimulation event in relation to the reliability of an example EXC neuron (black line). Following this, *post hoc* analysis was used to identify stimulation events that occurred within periods of reliable firing and unreliable firing (shaded purple and green, respectively). ***B***, Diagram of experimental setup. ***C***, Left, Representative example of an EXC neuron that is suppressed following PV activation. Blue line indicates the time of the stimulation event. Right, Change in firing rate for each PV stimulation event. To facilitate comparisons between movies and mice, all neurons were aligned to have a maximum reliability at 1 s. All shaded areas are 95% CI of the median. Yellow circles represent nonsignificant change (relative to 0) and were computed using

PV-to-SST activity, lag duration and the correlation strength between PV and SST-INs were all significant predictors of EXC neuron reliability ($p = 0.0038$, F test relative to constant model).

Our observation that peak SST activity is delayed relative to PV agrees with recent calcium imaging results showing that across many different cortical areas, SST-INs respond after PV-INs (Allen et al., 2017). Furthermore, in V1, sinusoidal gratings also elicit delayed SST-IN responses (Ma et al., 2010), albeit at a much shorter time scale. Possible mechanisms (not mutually exclusive) that could account for this delay include (1) pooling of inputs from EXC neurons (Karnani et al., 2016), and (2) inhibitory connections between SST and PV-INs. We took advantage of SXP mice to provide two additional pieces of evidence to support the latter claim. First, silencing SST-INs optically with ArchT strongly increased the PV-IN firing rate (Fig. 3*A*,*B*), confirming a strong inhibitory connection between SST and PV-INs. Second, optically activating SST-INs with ChR2, suppressed PV-INs and increased the duration of the temporal delay between PV and SST-INs (Fig. 3*C*–*D*). To discount an alternate hypothesis that these effects are caused by a polysynaptic circuit involving EXC neurons, we titrated our laser powers such that suppressing or activating SST-INs caused little change in the EXC neuron firing rate (see above, Materials and Methods). Therefore, these results suggest that the temporal delay is the result of the SST→PV circuit, which suppress PV-INs as SST activity ramps up.

SST and PV-INs bidirectionally modulate EXC neuron reliability

Our experiments in SXP mice revealed the surprising result that the strength of temporal interactions between PV and SST-INs, which is coordinated by the SST→PV circuit, varies with EXC neuron reliability. Therefore, it is possible that both SST-INs and PV-INs might work together to reduce variability. Using SST-Cre and PV-Cre mice crossed with Cre-dependent ChR2 mice (Ai32), we next asked how photoactivating each IN subtype specifically during epochs of either reliable or unreliable firing affected reliability. As the timing and duration of these epochs are heterogeneous within any given population, we had no way of estimating a priori when EXC neurons would respond reliably during a particular movie. To circumvent this issue, we developed an optical stimulation strategy to activate ChR2-expressing PV and SST-INs (PV-Cre and SST-Cre x Ai32) at 22 different time points that spanned the entire duration of a movie (Fig. 4*A*; see above, Materials and Methods). Specifically, we first created a distribution of stimulation events that spanned the duration of a movie, with the first and last events coincident with the onset and offset of the stimulus, respectively, and the remaining events occurring at fixed interval of 200 ms. Then, on every movie repetition (trial), we picked a stimulation event from this distribution in a pseudorandomized manner (Fig. 4*A*). Thereafter, with *post hoc* analysis, we focused primarily on stimulation events that coincided with epochs of either reliable or unreliable firing.

We first investigated the effect of perturbing PV-IN activity (Fig. 4*B*). These brief blue (473 nm) laser pulses were sufficient to reliably excite PV-INs at all time points during a movie (Fig. 4*C*). As expected, activating PV-INs suppressed EXC neurons shortly after laser onset. The magnitude of suppression was strongest when EXC neurons were most reliable and weakest when activity was unreliable (Fig. 4*D*). It is important to note that the epoch of most/least reliable firing occurs at different time points in the movie, and for the sake of visualization, we aligned reliability plots so that the maximum rate occurred at 1 s following stimulus onset (see above, Materials and Methods). Activating PV-INs significantly reduced the reliability of EXC neurons (Fig. 4*D*). In particular, increasing the strength of PV inhibition during epochs of reliable firing led to a ~20% reduction in EXC neuron reliability (Fig. 4*E*), whereas further increasing PV-IN activity during epochs of unreliable firing, when they are normally most active (Fig. 1), did not change reliability (Fig. 4*F*). It is important to note that this change in reliability was not because of an artifact of deconvolution, as we observed a similar decrease in EXC neuron reliability when we performed the same analysis using ΔF/F instead (Fig. 5*A*). Furthermore, we observed that this suppression lasted for ~600 ms, reflecting polysynaptic effects caused by activating a large number of PV-INs, and we restricted our analysis of reliability during this time period of maximum suppression (Fig. 5*C*,*D*).

These observed changes in reliability could be because of changes in either mean response rate (ΔRate) or between-trial variance (ΔVariance) or both. For example, a strong decrease in response rate, without a change in variability, could also reduce reliability. To quantify the effect these attributes had on ΔReliability, we used multivariate linear regression (model, ΔReliability ~ 1 + ΔRate + ΔVariance). Surprisingly, we did not observe a correlation between ΔRate and ΔReliability following PV-IN activation in either response epoch, as neurons that were suppressed more did not exhibit a larger decrease in reliability (Fig. 4*G*,*H*). Instead, the reduction in reliability following PV-IN activation during periods of reliable firing was strongly correlated with an increase in firing rate variance between the trials (ΔVariance, $p < 10^{-3}$ vs ΔRate, $p > 0.05$; t test). This implies that the change in reliability following PV-IN activation was because of an increase in variability rather than a change in rate.

Given the highly recurrent architecture of V1 layer 2/3, it is possible that in addition to EXC neurons, perturbing PV-INs would also affect SST-INs. To answer this question, we conditionally expressed a FlpO-dependent ChR2 in PV-INs and a Cre-dependent GCaMP6f in SST-INs in SXP mice (Fig. 4*I*). Surprisingly, regardless of when in the movie we activated PV-INs, we did not observe a suppression of SST-INs (Fig. 4*J*) or a change of SST-IN reliability (Fig. 4*K*). This result implies there is not an inhibitory PV→SST connection, and the reduction of EXC neuron rate is not sufficient to alter SST-IN activity. Importantly, this result implies that the reduction in EXC neuron reliability following PV activation is not because of a change in SST→EXC inhibition but rather because of direct PV→EXC inhibition.

As a control, we repeated these activation experiments in mice that expressed the red fluorescent protein tdTomato in

←

a permutation test; p values (Bonferroni-corrected rank-sum test) compare changes in firing rate between epochs of reliable versus unreliable responses (shaded bars). ***D***, Change in EXC reliability for each stimulation event. ***E***, Left, Representative raster plot of an EXC neuron showing a reduction in reliability following PV activation during the reliable firing epoch. Right, Box-whisker plots summarizing the effect of PV activation on EXC neuron reliability. Each dot is pooled data from one population; p value computed using Bonferroni-corrected Wilcoxon rank-sum test. ***F***, Same as ***E*** but shows no change in reliability when PV-INs are activated during epochs of unreliable firing. ***G***, ***H***, Scatter plots quantifying the relationship between ΔReliability and a change in rate (ΔRate, left) or a change in between-trial variability (ΔVariance, right). Error bars indicate 95% CI of the median; p values computed from multivariate linear regression analysis. ***I***, Diagram describing method to study the effect of PV activation on SST-INs. ***J***, Left, Representative SST-IN that shows no change following PV activation. Right, No change in SST rate for all PV activation events. ***K***, No change in SST reliability for all PV activation events.

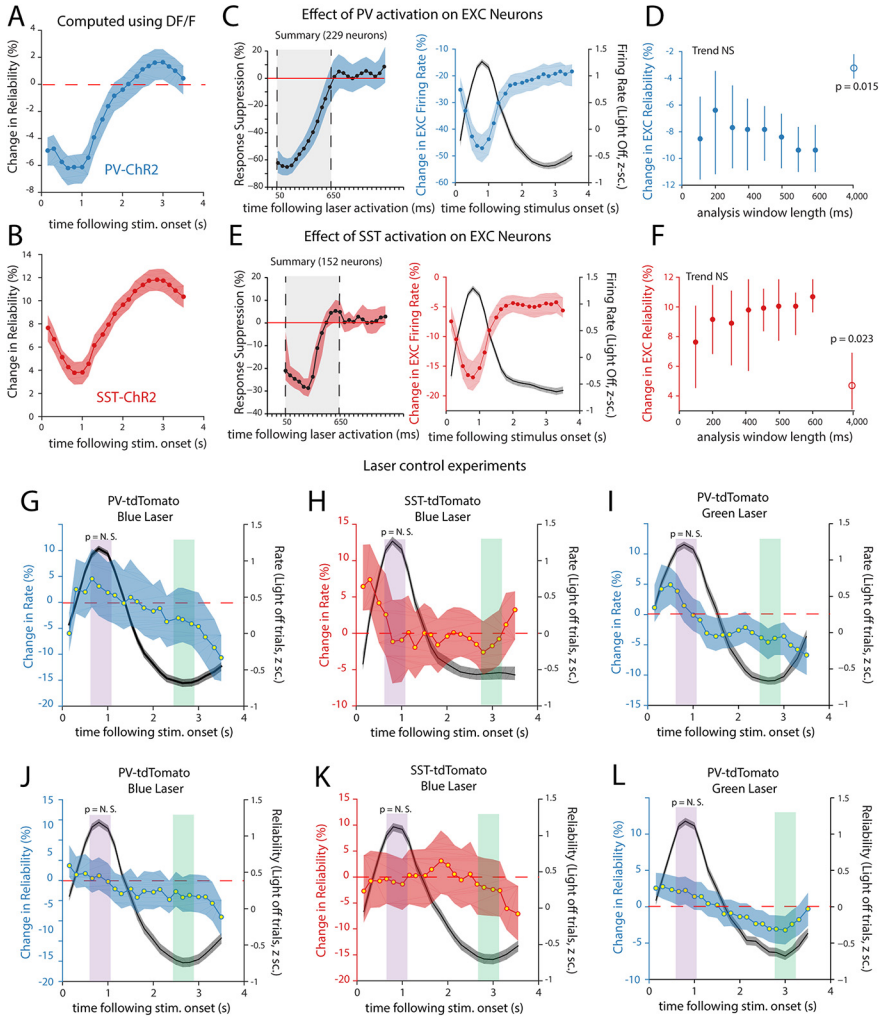

Figure 5. Deconvolution and analysis window length does not affect reliability; change in rate and reliability is not because of stimulation laser artifacts. ***A***, Change in reliability measured using DF/F without deconvolution for PV neurons. ***B***, Change in reliability measured using DF/F without deconvolution for SST neurons. Data same as Figures 4 and 6. ***C***, Percent change in EXC neuron response following laser activation of PV-INs. All data analysis was limited to a 600 ms window indicated by the gray box. During this period, the laser maximally suppresses EXC neurons. ***D***, Plot of change in EXC reliability following PV activation at stimulus onset over different analysis window lengths. We found that changing the window length within 50 (1 frame) to 600 ms (12 frames) following laser offset did not significantly affect the reduction in EXC reliability caused by PV activation. The effect, however, was significantly diminished when the entire 4 s stimulus-on period (open circle) was included in the analysis. This is mainly because of the fact that PV-INs stop exerting an inhibitory effect on EXC neurons after 650 ms as shown in ***C***. ***E***, ***F***, Same as ***C*** and ***D*** but for SST-IN activation instead. Again, changing the duration of the analysis window does not affect the increase in EXC reliability caused by SST activation. Data in ***C–F*** indicate mean ± SEM for stimulation at stimulus onset. Analysis of other stimulation epochs yielded qualitatively similar results. All shaded areas are 95% CI of median. ***G–I***, No significant change in response rate in tdTomato-expressing mice following stimulation with either blue (***G***, ***H***) or green laser (***I***; see above, Material and Methods). ***J–L***, No significant change in reliability in the same tdTomato-expressing mice. Data pooled from PV-tdTomato (blue laser) = three mice (120 neurons), PV-tdTomato (green laser) = three mice (102 neurons), SST-tdTomato = three mice (98 neurons). All p values are nonsignificant (permutation test). Shaded areas indicate 95% CI of median. N.S., non-significant.

either PV or SST-INs instead of ChR2. In these mice, we found no significant change in either response rate or reliability of EXC neurons following laser stimulation (Fig. 5*G–L*). Additionally, inferring firing rates via deconvolution did not influence our reliability calculation as neurons that had reliable calcium transients also had reliable inferred rates (Fig. 5*A–F*).

In contrast to PV-INs, activating SST-INs had a much weaker suppressive effect on EXC neurons (Fig. 6*A*,*B*; $p < 10^{-4}$, one-way Kruskal–Wallis ANOVA relative to PV-ChR2). This was in part because of a disinhibitory effect caused by a lifting of PV inhibition following SST activation as ~27% of the neurons (8 of 20 populations) showed an increased rate following SST activation. Also in contrast to PV activation, increasing the strength of SST inhibition increased the reliability of EXC neurons (Figs. 5*B*, 6*C*). This effect was most significant when SST-INs were activated during epochs of unreliable firing (Fig. 6*E*). This increase in reliability was correlated with a strong reduction in trial-to-trial variance and a modest increase in response rate (Fig. 6*G*). Multivariate linear regression confirmed that both variables had a significant effect on ΔReliability (ΔVariance, $p < 10^{-5}$; ΔRate, $p < 10^{-2}$; t test). Interestingly, further increasing the activity of SST-INs during periods of reliable firing did not alter EXC neuron reliability and only marginally reduced trial-to-trial variance (Fig. 6*D–F*).

Using SXP mice, we found that SST activation strongly suppressed PV-INs, regardless of when the stimulation occurred during the movie (Fig. 6*H*,*I*). Surprisingly, unlike EXC neurons, activating SST-INs further reduced the reliability of PV-INs (Fig. 6*J*). Therefore, increasing SST inhibition influences both EXC neuron reliability and the dynamics of PV-IN inhibition.

Together, these results demonstrate complementary roles of PV and SST-INs in modulating EXC neuron reliability (Fig. 6*K*,*L*). In particular, increasing PV inhibition when EXC neurons are reliable decreases reliability by increasing variability between trials but does not alter SST-IN dynamics. On the other hand, increasing SST inhibition when EXC neurons are unreliable increases reliability by a combined effect of decreased variability and, to a lesser extent, a disinhibitory increase in response rate caused by a suppression of PV-INs.

Computational model predicts that SST-INs increase reliability by suppressing PV-INs

How do SST-INs increase EXC neuron reliability? Given the complementary relationship between PV and SST-INs, we hypothesized that the inhibitory SST→PV circuit might play a role in coordinating activity between these INs and consequently modulating EXC neuron reliability. To test this hypothesis, we developed a computational model of V1 microcircuit dynamics that simulated the mean firing rate of different neural subtypes (Fig. 7*A*; see above, Materials and Methods). Our model comprised three rate-based units (EXC, SST, PV), which were interconnected through connectivity parameters (Kuchibhotla et al., 2017). EXC, SST, and PV units in our model received visual input from a bank of LNP units (Paninski, 2004), each with Gabor-like spatiotemporal

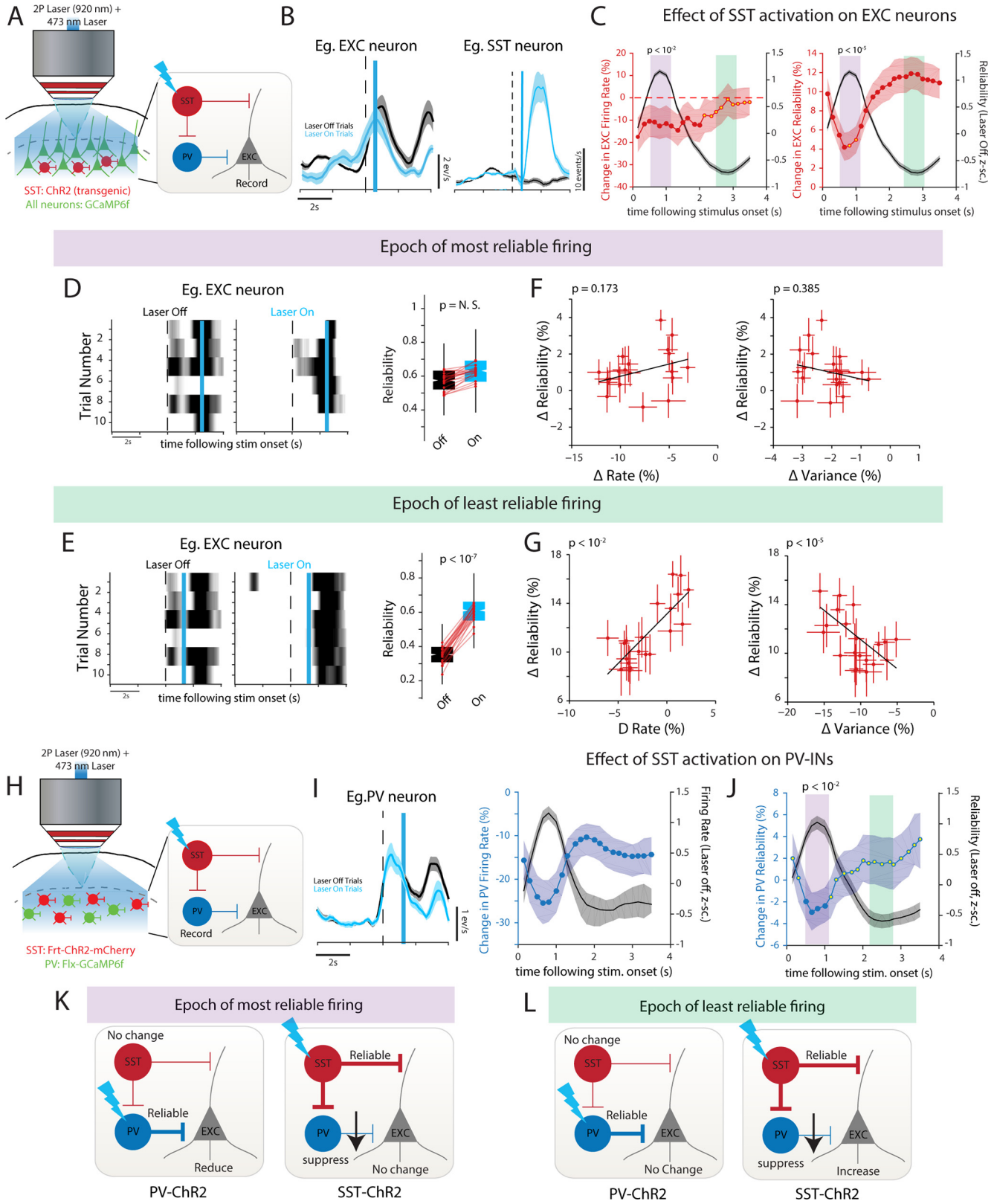

Figure 6. Increasing SST-IN activity increases EXC neuron reliability. ***A***, Diagram of experimental setup. ***B***, Left, Representative EXC neuron that shows a modest decrease in firing rate following SST activation (blue bar). Right, Change in firing rate for each SST stimulation event shown in relation to EXC neuron reliability on light-off trials. ***C***, Change in EXC neuron reliability for each SST stimulation event. ***D***, Representative raster plot of an EXC neuron and box-whisker plot showing no change in reliability following SST activation during epoch of most reliable firing. ***E***, Same as ***D*** but showing that SST activation during epoch of least reliable firing can increase EXC neuron reliability. ***F***, ***G***, Scatter plots quantifying the relationship between ΔReliability and a change in rate (ΔRate, left) or a change in between-trial variability (ΔVariance, right). Error bars are 95% CI of the median; *p* values computed from multivariate linear regression analysis. Data in ***B–G*** are from 8 SST-ChR2 mice (622 neurons, 19 populations). ***H***, Diagram describing method to study the SST activation on PV-INs. ***I***, Left, Representative PV-IN that is suppressed following SST activation. Right, PV-IN firing rate is significantly suppressed for all SST activation events. ***J***, SST activation reduces the reliability of PV-INs. Data in same format as Figure 4 and are from 4 SXP mice (372 PV neurons). ***K***, ***L***, Diagram summarizing photoactivation results. N.S., non-significant.

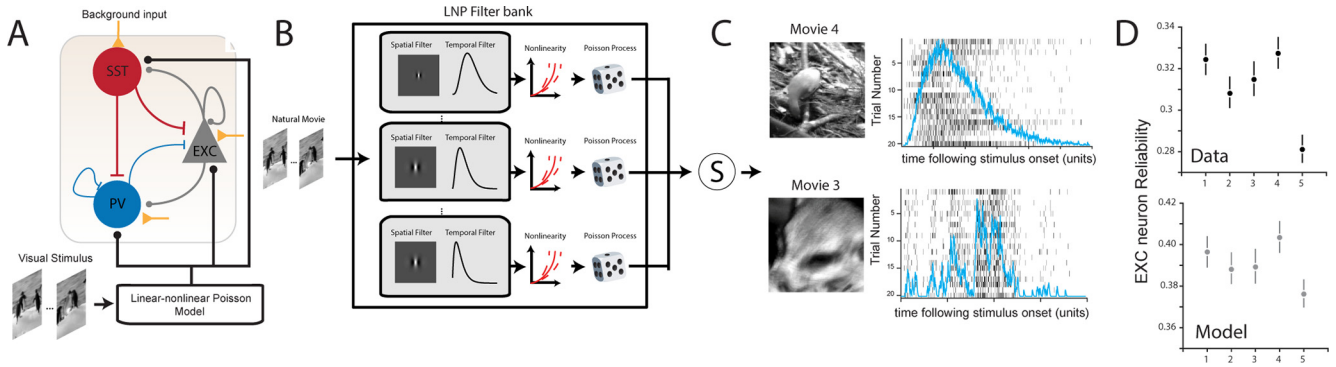

Figure 7. Computational model accurately captures temporal dynamics and variability to natural movies. ***A***, Diagram illustrating connectivity among the three major units simulated in this model. Round connections indicate excitatory synapses, whereas blunt connections indicate inhibitory synapses. ***B***, See above, Material and Methods for details of the LNP model. ***C***, Example input spike trains produced by the LNP model along with estimated firing rates (blue lines, normalized to maximum) to two different natural movies. Note that the model captures the different temporal properties of each movie, and as a result produces different inputs for each movie. For each movie, these spike trains are summed and used as an input to either EXC, PV, and SST units. ***D***, The LNP model is able to recapitulate the moviewise trend in EXC neuron reliability observed in the experimental data (black dots). The gray dots are the average reliability of EXC units in the model (from 500 simulations; see above, Materials and Methods). Error bars indicate SEM.

receptive fields of different orientations and spatial frequencies (Fig. 7*B*; see above, Materials and Methods). Additionally, each unit in the model also received Poisson noise, which modeled background inputs. As a result, each unit in our model had both an independent (uncorrelated) and a shared source of variability. Because of the stochastic nature of the Poisson process, each trial produced visual inputs, which differed in both the number and timing of spikes. As previously reported (Rikhye and Sur, 2015), this method allowed us to accurately capture both the temporal dynamics and reliability of the same movies that we used in our experiments (Fig. 7*C*,*D*).

First, we asked whether this model could recapitulate and explain the relationship between PV-SST delay and EXC reliability (Fig. 2). As in our experimental data, SST units in our model also lagged behind PV units with a variable delay (Fig. 8*A*). Parametrically reducing the strength of the SST→PV connection from maximum to 0% (no connection) reduced the duration of the lag (Fig. 8*B*). This is consistent with the proposal that the temporal relationship observed between PV-SST pairs *in vivo* is because of the inhibitory SST→PV circuit. Also similar to our experimental results, we observed a correlation between the duration of the PV-SST lag and EXC reliability in that models with higher EXC reliability also had more delayed SST peak activity relative to PV peak activity (Fig. 8*C*). Removing the SST→PV connection abolished this relationship, increased PV unit activity and reduced EXC neuron reliability (Fig. 8*C*). We performed multivariate regression analysis to identify the variables that contributed most to this temporal relationship. Interestingly, the strength of the SST→PV connection and the activity fraction of SST units to PV units were the biggest predictors of the lag duration. This implies that conditions that strongly recruit SST-INs, such as reliable EXC neuron firing, will increase the dynamics of joint PV-SST activity. Therefore, intact joint PV-SST dynamics seems to be necessary for reliable EXC neuron firing.

Next, we asked whether this model could predict the results of our photostimulation experiments. We simulated optical activation by injecting a brief train of depolarizing current into SST units with similar temporal properties as in our experiments. As in our experiments, increasing the strength of SST inhibition increased EXC reliability and suppressed PV units (Fig. 8*D*–*F*). Notably, the model demonstrates that SST activation is most effective at increasing reliability when EXC units were unreliable. We found a strong correlation between the change in EXC reliability and the change in PV unit activity in that large increases in reliability were accompanied with a strong suppression of PV unit activity (Fig. 8*E*). Changes in the EXC unit firing rate, on the other hand, were poorly predictive of the increase in reliability (Fig. 8*F*). Interestingly, we observed that gradually reducing the strength of the SST→PV connection reduced the SST-induced suppression of PV units (Fig. 8*H*) and increased EXC variability (Fig. 8*I*, left). Our model also correctly predicted a decrease in reliability following PV activation (Fig. 8*G*). This decrease in EXC reliability was independent of the strength of the SST→PV connection (Fig. 8*I*, right; $p = 0.54$, Cochrane–Armitage test for trend). Together, these simulation results suggest that SST-INs increase reliability primarily by suppressing PV-INs.

Furthermore, these results raise the possibility that PV units might be injecting noise into EXC units. In support of this idea, transiently suppressing PV units by injecting a brief hyperpolarizing current increased reliability when EXC units were unreliable but decreased reliability when EXC units were reliable (Fig. 8*J*). Therefore, our model supports the hypothesis that SST-INs reduce variability in EXC neurons by suppressing PV-INs.

Suppressing PV-INs improves EXC neuron reliability

The main prediction of our model is that the increase in EXC reliability is caused by an SST-induced suppression of PV-INs. To examine this prediction *in vivo*, we directly suppressed PV-INs in mice that transgenically expressed Arch (PV-Cre x Ai35 mice; Fig. 9*A*). As expected, Arch-expressing PV-INs were strongly suppressed following green laser stimulation with a latency that was comparable to SST activation (Fig. 9*B*). This method therefore mimicked the suppressive effect that SST activation had on PV-INs while avoiding the direct effect of SST inhibition on EXC neurons.

Because of a transient lifting of somatic inhibition, optically suppressing PV-INs strongly increased response rates when EXC neurons were most active (Fig. 9*C*). Despite this increase in response rate, suppressing PV-INs during epochs of reliable firing did not significantly change either reliability or between-trial variance (Fig. 9*D*,*E*). On the other hand, reducing PV inhibition during epochs of unreliable firing increased EXC neuron reliability (Fig. 9*F*), similar to SST activation. This change in reliability was primarily because of a reduction in between-trial variance as

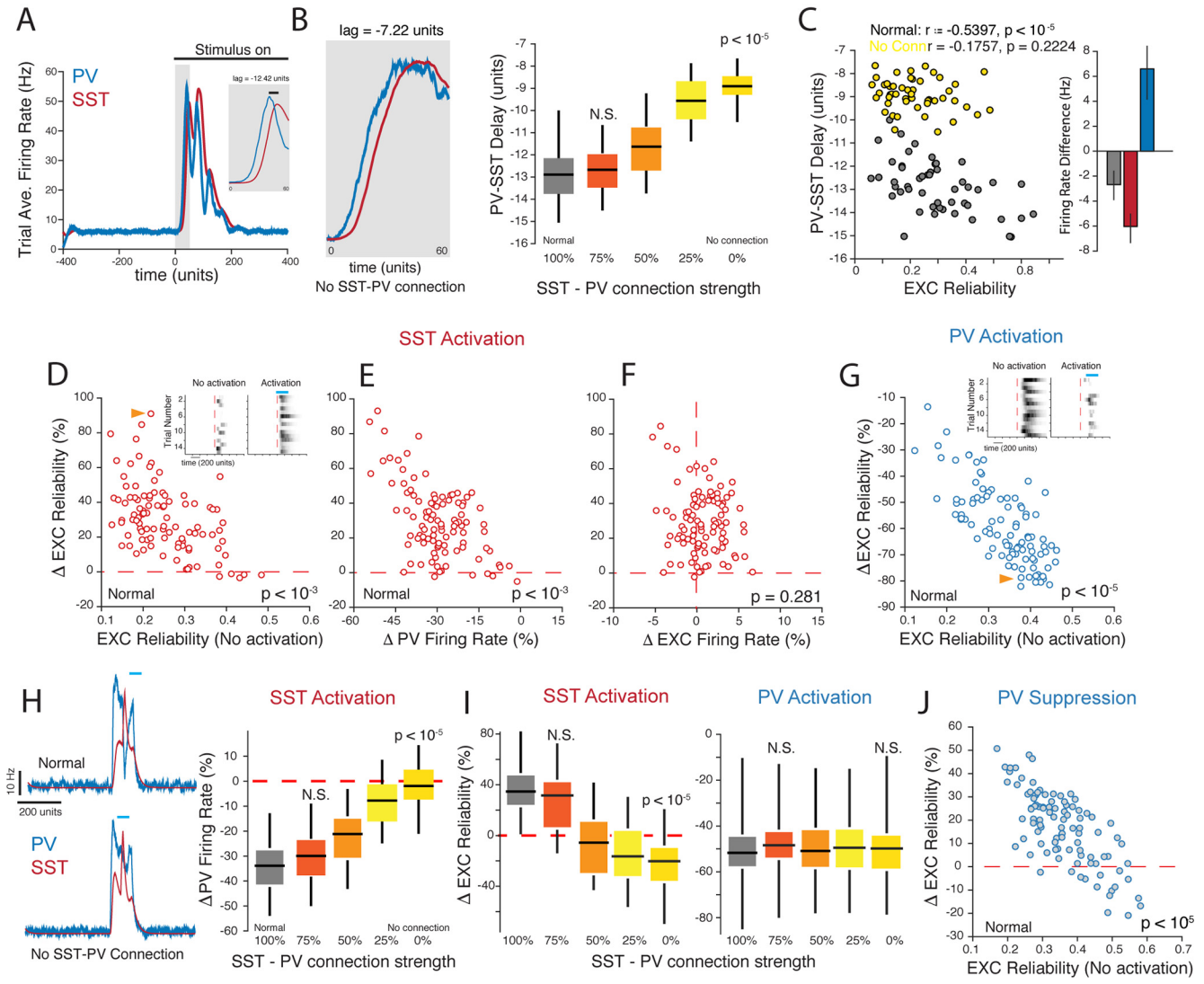

Figure 8. Computational model predicts that SST-INs increase reliability by suppressing PV-Ins. ***A***, Representative simulation showing the response of PV and SST units to a natural movie. Inset, Zoomed view of the onset dynamics to highlight the temporal lag between PV and SST units. ***B***, The delay between PV and SST units is reduced when the SST→PV connection is removed. Box-whisker plots quantify the change in time lag between PV and SST units caused by parametrically reducing the strength of the SST→PV connection from normal weight to zero (no connection). Data are pooled from 100 simulations each with randomly drawn connection weights; *p* value computed using Kruskal–Wallis one-way ANOVA relative to the model with normal SST→PV connection. ***C***, Left, Significant correlation between PV-SST delay duration and EXC unit reliability for the normal model, which is lost when the SST→PV connection is cut. Right, Removing the SST→PV circuit increases PV unit firing rate while suppressing SST and EXC units. Error bar indicates SEM over simulations. ***D***, Model predicts that activating SST activation during epoch of unreliable firing will increase the reliability of EXC units. Inset, Representative raster plot of an EXC unit (orange arrow). ***E***, Large changes in EXC unit reliability are associated with a large decrease in PV unit firing rate. ***F***, Scatter plot showing no significant relationship between the changes in EXC unit reliability and firing rate following SST unit activation. Each data point is an independent model simulation (see above, Materials and Methods). ***G***, Model predicts that PV activation will reduce reliability. ***H***, SST-induced suppression is reduced when the SST→PV connection is cut. Box-whisker plot showing the change in PV firing rate as the SST→PV connection strength is varied; *p* value computed using Kruskal–Wallis one-way ANOVA relative to the model with normal SST→PV connection. ***I***, Left, Box-whisker plot showing that the change in EXC unit reliability induced by SST activation varies as the connection strength is changed. Right, The effect of PV activation on EXC reliability is independent of the SST→PV connection strength. ***J***, Suppressing PV units will result in an increase in variability. All data points are an independent simulation in which a natural movie is repeated 30 times. To test robustness, we repeated each simulation 100 times, each with randomly drawn connection weights; *p* values in the scatter plots are computed from linear regression (see above, Materials and Methods).

ΔRate was not a statistically significant predictor (Fig. 9*G*,*H*). Under control conditions, the green laser alone was unable to change either the firing rate or the reliability of EXC neurons (Fig. 5*I*–*L*). Therefore, transiently reducing PV inhibition with Arch had a similar effect on EXC neuron reliability as increased SST-IN activity, confirming our prediction.

Discussion

Reducing trial-to-trial variability within cortical neuron networks is critical for accurate sensory information processing; however, the underlying neural mechanisms remain unknown. In this study, we used novel double transgenic mice and all-optical physiology to reveal a previously unknown role of the SST→PV circuit in bidirectionally modulating the reliability of EXC neurons to naturalistic stimuli in mouse V1.

Our experiments reveal that a sufficient condition for reliable sensory processing is active SST-INs and weaker/suppressed PV-INs and that this mutual antagonism is maintained through the inhibitory action of the SST→PV circuit. Surprisingly, a study identified PV-INs, but not SST-INs, as critical regulators of reliability (Zhu et al., 2015). A key reason for this difference is that

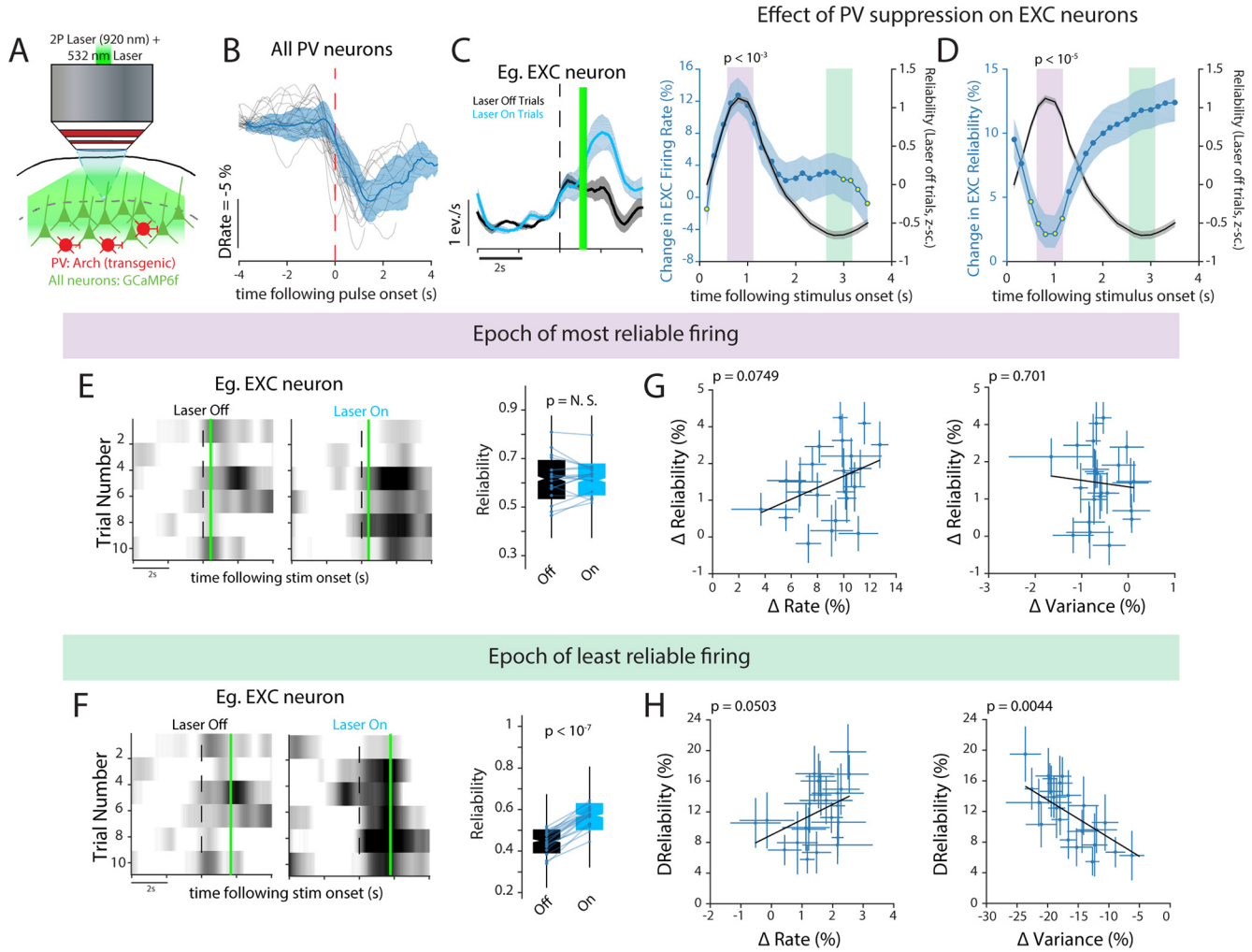

Figure 9. Suppressing PV-INs increases EXC neuron reliability. ***A***, Experimental setup. ***B***, Arch activation transiently suppresses PV-INs with short latency following laser onset. ***C***, Left, Suppressing PV-INs transiently increases the response rate of EXC neurons. Right, Change in firing rate for all PV suppression event. ***D***, Change in EXC neuron reliability, aligned to reliability on Laser-off trials. ***E***, Left, Representative raster plot of an EXC neuron showing no change in reliability following PV suppression during epoch of most reliable firing. Right, Box-whisker plot summarizing the effect of PV suppression. Each dot represents the median reliability from each imaged population; *p* value computed using Bonferroni-corrected rank-sum test. ***F***, Same as ***E***, but showing an increase in reliability following PV suppression during epoch of least reliable firing. ***G***, Changes in reliability that occur when PV-INs are suppressed during epoch of most reliable firing are weak because of ΔRate (left) but not ΔVariance (right). Each data point in ***I*** and ***J*** shows median change for each imaged population. Error bars indicate 95% CI of the median; *p* values computed from multivariate linear regression analysis. ***H***, Same as ***G*** but shows that the increase in reliability is strongly associated with a reduction in variance but not a change in rate. Data in this figure are from 8 mice (634 neurons, 22 populations).

Zhu et al. suppressed PV-INs for a much longer duration than our study (6 s vs 110 ms). The main advantage of our photostimulation method is that it allowed us to show that the effect of SST and PV-INs on modulating EXC variability is highly dependent on the current reliability of EXC neurons. Namely, SST-INs were less effective at increasing reliability during epochs of reliable firing, whereas PV-INs were less effective at reducing reliability during epochs of unreliable firing. Furthermore, our model simulations showed that without the SST→PV circuit, SST-IN activation decreased reliability. Our data therefore supports the idea that SST and PV-INs must provide temporally restricted inhibition in relation to EXC neurons to change variability. Long-term suppression of PV and SST-INs would likely disrupt this relationship between these interneurons. Therefore, our findings, together with others (El-Boustani et al., 2014; Lee et al., 2014; Seybold et al., 2015), underscores the importance of using precisely timed perturbations to study the dynamics of cortical inhibition. Importantly, we demonstrate that the responsibility of modulating response reliability does not lie exclusively with one neuronal subtype; instead, it is the co-operative dynamics between SST and PV-INs that is important for controlling the temporal fidelity of sensory processing.

Previous work has shown that feed forward inhibition, acting through fast-spiking PV-INs, plays a critical role in shaping the temporal fidelity of EXC neurons. For example, the delay between inhibition and excitation creates a temporal integration window (Pouille and Scanziani, 2001; Wehr and Zador, 2003), and variations in the duration of this window change the spiking precision of EXC neurons to sensory stimulation (Gabernet et al., 2005). However, sparse activity patterns, which are common during natural scene stimulation (Yen et al., 2007), strongly recruit feedback or recurrent inhibition from SST-INs and only weakly recruit PV-INs (Tan et al., 2008). Our work reconciles these observations and demonstrates how the SST→PV circuit allows recurrent inhibition to modulate the strength of feedforward inhibition during epochs of reliable coding under naturalistic conditions.

A potential biophysical function of the SST→PV circuit may be to maximize the signal-to-noise ratio of EXC neurons by minimizing noise in the synaptic inputs and maximizing spiking at the soma. Specifically, SST-INs are ideally poised to alter synaptic integration in EXC neurons by altering the active properties of dendrites in a branch-specific manner (Lovett-Barron et al., 2012; Palmer et al., 2012; Chiu et al., 2013; Bloss et al., 2016; Yang et al., 2016). This, in turn, would allow only the most reliable inputs to be integrated (Branco and Häusser, 2011; Egger et al., 2015). Our observation that SST-INs lag behind PV-INs during periods of reliable firing implies that during these epochs, inhibition is routed away from the soma and into the dendrites. Similar results have been observed in the hippocampus and the barrel cortex, where inhibitory inputs shift from the soma to the dendrite depending on the firing rate of the neuron (Pouille and Scanziani, 2004; Tan et al., 2008). Computational models have shown that this mechanism allows SST-INs to adaptively adjust the integration threshold at the soma, which in turn can increase the robustness of spiking in the presence of stochastic inputs (Fontaine et al., 2014; Huang et al., 2016). Future studies could be aimed at using our dual labeling technique to further characterize the interactions between PV and SST INs during times scales more relevant to synaptic integration. There is also a growing body of evidence that basal forebrain cholinergic inputs (Chen et al., 2015), and long-range excitatory inputs from other cortical areas (Zhang et al., 2014; Ibrahim et al., 2016), can modulate SST-IN activity. Therefore, the SST→PV circuit is an appropriate target for top-down influences, such as arousal and attention, to alter local computations in V1 by changing EXC neuron variability. This notion is further bolstered by several findings that both cholinergic modulation and higher cortical feedback, which also change response reliability and selectivity, can improve stimulus discriminability (Pinto et al., 2013; Zhang et al., 2014; Chen et al., 2015; Kuchibhotla et al., 2017; Zhang et al., 2020) by modulating the local excitatory-inhibitory (E-I) dynamics in a cell-type specific way (Hertäg and Sprekeler, 2019).

The impact that sensory processing variability has on visual perception remains debated. Although several studies have established a relationship between trial-to-trial fluctuations in sensory neurons and perceptual decisions (Britten et al., 1996; Nienborg et al., 2012), it is still unclear if these fluctuations can be filtered out at later processing stages (Moldakarimov et al., 2015) and how this affects perception. One important follow-up to our study would be to investigate the effect that these precisely timed manipulations have on visual perception (Song et al., 2020).

In conclusion, our study establishes that PV and SST-INs have complementary roles in controlling neuronal response reliability. The cooperative action of these INs provides a powerful computational mechanism by which response variability can be titrated based on task demands (Deneve and Chalk, 2016) and internal state to improve the coding of stimulus information. In addition to the visual system, this strategy could also be active in other cortical areas to effectively gate the flow of information.

References

Adesnik H, Bruns W, Taniguchi H, Huang ZJ, Scanziani M (2012) A neural circuit for spatial summation in visual cortex. Nature 490:226–231.

Ali F, Kwan AC (2020) Interpreting *in vivo* calcium signals from neuronal cell bodies, axons, and dendrites: a review. Neurophotonics 7:011402.

Allen WE, Kauvar IV, Chen MZ, Richman EB, Yang SJ, Chan K, Gradinaru V, Deverman BE, Luo L, Deisseroth K (2017) Global representations of goal-directed behavior in distinct cell types of mouse neocortex. Neuron 94:891–907.e6.

Atallah BV, Bruns W, Carandini M, Scanziani M (2012) Parvalbumin-expressing interneurons linearly transform cortical responses to visual stimuli. Neuron 73:159–170.

Averbeck BB, Latham PE, Pouget A (2006) Neural correlations, population coding and computation. Nat Rev Neurosci 7:358–366.

Azouz R, Gray CM (1999) Cellular mechanisms contributing to response variability of cortical neurons *in vivo*. J Neurosci 19:2209–2223.

Berens P, Freeman J, Deneux T, Chenkov N, McColgan T, Speiser A, Macke JH, Turaga SC, Mineault P, Rupprecht P, Gerhard S, Friedrich RW, Friedrich J, Paninski L, Pachitariu M, Harris KD, Bolte B, Machado TA, Ringach D, Stone J, et al. (2018) Community-based benchmarking improves spike rate inference from two-photon calcium imaging data. PLoS Comput Biol 14:e1006157.

Bloss EB, Cembrowski MS, Karsh B, Colonell J, Fetter RD, Spruston N (2016) Structured dendritic inhibition supports branch-selective integration in CA1 pyramidal cells. Neuron 89:1016–1030.

Bondy AG, Haefner RM, Cumming BG (2018) Feedback determines the structure of correlated variability in primary visual cortex. Nat Neurosci 21:598–606.

Bonin V, Histed MH, Yurgenson S, Reid RC (2011) Local diversity and fine-scale organization of receptive fields in mouse visual cortex. J Neurosci 31:18506–18521.

Branco T, Häusser M (2011) Synaptic integration gradients in single cortical pyramidal cell dendrites. Neuron 69:885–892.

Britten KH, Newsome WT, Shadlen MN, Celebrini S, Movshon JA (1996) A relationship between behavioral choice and the visual responses of neurons in macaque MT. Vis Neurosci 13:87–100.

Chen N, Sugihara H, Sur M (2015) An acetylcholine-activated microcircuit drives temporal dynamics of cortical activity. Nat Neurosci 18:892–902.

Chiu CQ, Lur G, Morse TM, Carnevale NT, Ellis-Davies GCR, Higley MJ (2013) Compartmentalization of GABAergic inhibition by dendritic spines. Science 340:759–762.

Cohen MR, Maunsell JHR (2009) Attention improves performance primarily by reducing interneuronal correlations. Nat Neurosci 12:1594–1600. doi:10.1038/nn.2439

Cottam JCH, Smith SL, Häusser M (2013) Target-specific effects of somatostatin-expressing interneurons on neocortical visual processing. J Neurosci 33:19567–19578.

Dana H, Mohar B, Sun Y, Narayan S, Gordus A, Hasseman JP, Tsegaye G, Holt GT, Hu A, Walpita D, Patel R, Macklin JJ, Bargmann CI, Ahrens MB, Schreiter ER, Jayaraman V, Looger LL, Svoboda K, Kim DS (2016) Sensitive red protein calcium indicators for imaging neural activity. Elife 5:12727.

Danielson NB, Zaremba JD, Kaifosh P, Bowler J, Ladow M, Losonczy A (2016) Sublayer-specific coding dynamics during spatial navigation and learning in hippocampal area CA1. Neuron 91:652–665.

Deneve S, Chalk M (2016) Efficiency turns the table on neural encoding, decoding and noise. Curr Opin Neurobiol 37:141–148.

Dombeck DA, Khabbaz AN, Collman F, Adelman T, Tank DW (2007) Imaging large-scale neural activity with cellular resolution in awake, mobile mice. Neuron 56:43–57.

Egger R, Schmitt AC, Wallace DJ, Sakmann B, Oberlaender M, Kerr JND (2015) Robustness of sensory-evoked excitation is increased by inhibitory inputs to distal apical tuft dendrites. Proc Natl Acad Sci U S A 112:14072–14077.

El-Boustani S, Wilson NR, Runyan CA, Sur M (2014) El-Boustani et al. reply. Nature 508:E3–4.

Engel TA, Steinmetz NA, Gieselmann MA, Thiele A, Moore T, Boahen K (2016) Selective modulation of cortical state during spatial attention. Science 354:1140–1144.

Evans M, Petersen RD, Humphries MD (2019) On the use of calcium deconvolution algorithms in practical contexts. bioRxiv 871137.

Ferguson KA, Cardin JA (2020) Mechanisms underlying gain modulation in the cortex. Nat Rev Neurosci 21:80–92.

Fontaine B, Peña JL, Brette R (2014) Spike-threshold adaptation predicted by membrane potential dynamics *in vivo*. PLoS Comput Biol 10:e1003560.

Frégnac Y, Bathellier B (2015) Cortical correlates of low-level perception: from neural circuits to percepts. Neuron 88:110–126.

Froudarakis E, Berens P, Ecker AS, Cotton RJ, Sinz FH, Yatsenko D, Saggau P, Bethge M, Tolias AS (2014) Population code in mouse V1 facilitates readout of natural scenes through increased sparseness. Nat Neurosci 17:851–857.

Gabernet L, Jadhav SP, Feldman DE, Carandini M, Scanziani M (2005) Somatosensory integration controlled by dynamic thalamocortical feed-forward inhibition. Neuron 48:315–327.

Goard MJ, Pho GN, Woodson J, Sur M (2016) Distinct roles of visual, parietal, and frontal motor cortices in memory-guided sensorimotor decisions. Elife 5:13764.

Haider B, McCormick DA (2009) Rapid neocortical dynamics: cellular and network mechanisms. Neuron 62:171–189.

Haider B, Krause MR, Duque A, Yu Y, Touryan J, Mazer JA, McCormick DA (2010) Synaptic and network mechanisms of sparse and reliable visual cortical activity during nonclassical receptive field stimulation. Neuron 65:107–121.

He M, Tucciarone J, Lee S, Nigro MJ, Kim Y, Levine JM, Kelly SM, Krugikov I, Wu P, Chen Y, Gong L, Hou Y, Osten P, Rudy B, Huang ZJ (2016) Strategies and tools for combinatorial targeting of GABAergic neurons in mouse cerebral cortex. Neuron 92:555.

Hertäg L, Sprekeler H (2019) Amplifying the redistribution of somato-dendritic inhibition by the interplay of three interneuron types. PLoS Comput Biol 15:e1006999.

Huang C, Resnik A, Celikel T, Englitz B (2016) Adaptive spike threshold enables robust and temporally precise neuronal encoding. PLoS Comput Biol 12:e1004984.

Ibrahim LA, Mesik L, Ji X-Y, Fang Q, Li H-F, Li Y-T, Zingg B, Zhang LI, Tao HW (2016) Cross-modality sharpening of visual cortical processing through layer-1-mediated inhibition and disinhibition. Neuron 89:1031–1045.

Isaacson JS, Scanziani M (2011) How inhibition shapes cortical activity. Neuron 72:231–243.

Karnani MM, Jackson J, Ayzenshtat I, Tucciarone J, Manoocheri K, Snider WG, Yuste R (2016) Cooperative subnetworks of molecularly similar interneurons in mouse neocortex. Neuron 90:86–100.

Kayser C, Einhäuser W, König P (2003) Temporal correlations of orientations in natural scenes. Neurocomputing 52-54:117–123.

Kerlin AM, Andermann ML, Berezovskii VK, Reid RC (2010) Broadly tuned response properties of diverse inhibitory neuron subtypes in mouse visual cortex. Neuron 67:858–871.

Khan AG, Hofer SB (2018) Contextual signals in visual cortex. Curr Opin Neurobiol 52:131–138.

Kohn A, Coen-Cagli R, Kanitscheider I, Pouget A (2016) Correlations and neuronal population information. Annu Rev Neurosci 39:237–256.

Kuchibhotla KV, Gill JV, Lindsay GW, Papadoyannis ES, Field RE, Sten TAH, Miller KD, Froemke RC (2017) Parallel processing by cortical inhibition enables context-dependent behavior. Nat Neurosci 20:62–71.

Kwan AC, Dan Y (2012) Dissection of cortical microcircuits by single-neuron stimulation *in vivo*. Curr Biol 22:1459–1459.

Lawrence H, Ledochowitsch P, Knoblich U, Lecoq J, Murphy GJ, Reid RC, de Vries SEJ, Koch C, Zeng H, Buice MA, Waters J, Li L (2021) Relationship between simultaneously recorded spiking activity and fluorescence signal in GCaMP6 transgenic mice. eLife 10:e51675.

Lee S-H, Kwan AC, Dan Y (2014) Interneuron subtypes and orientation tuning. Nature 508:E1–2.

Litwin-Kumar A, Rosenbaum R, Doiron B (2016) Inhibitory stabilization and visual coding in cortical circuits with multiple interneuron subtypes. J Neurophysiol 115:1399–1409.

Liu T, Cable D, Gardner JL (2018) Inverted encoding models of human population response conflate noise and neural tuning width. J Neurosci 38:398–408.

Lovett-Barron M, Turi GF, Kaifosh P, Lee PH, Bolze F, Sun X-H, Nicoud J-F, Zemelman BV, Sternson SM, Losonczy A (2012) Regulation of neuronal input transformations by tunable dendritic inhibition. Nat Neurosci 15:423–430.

Ma W, Liu B, Li Y, Huang ZJ, Zhang LI, Tao HW (2010) Visual representations by cortical somatostatin inhibitory neurons–selective but with weak and delayed responses. J Neurosci 30:14371–14379.

Madisen L, Mao T, Koch H, Zhuo J, Berenyi A, Fujisawa S, Hsu Y-WA, Garcia AJ, Gu X, Zanella S, Kidney J, Gu H, Mao Y, Hooks BM, Boyden ES, Buzsáki G, Ramirez JM, Jones AR, Svoboda K, Han X, et al (2012) A toolbox of Cre-dependent optogenetic transgenic mice for light-induced activation and silencing. Nat Neurosci 15:793–802.

Meng CB, Zhou JH, Papaneri A, Peddada T, Xu KR, Cui GH (2018) Spectrally resolved fiber photometry for multi-component analysis of brain circuits. Neuron 98:707–717.e4.

Minces V, Pinto L, Dan Y, Chiba AA (2017) Cholinergic shaping of neural correlations. Proc Natl Acad Sci U S A 114:5725–5730.

Moldakarimov S, Bazhenov M, Sejnowski TJ (2015) Feedback stabilizes propagation of synchronous spiking in cortical neural networks. Proc Natl Acad Sci U S A 112:2545–2550.

Murayama M, Pérez-Garci E, Nevian T, Bock T, Senn W, Larkum ME (2009) Dendritic encoding of sensory stimuli controlled by deep cortical interneurons. Nature 457:1137–1141.

Nienborg H, Cohen MR, Cumming BG (2012) Decision-related activity in sensory neurons: correlations among neurons and with behavior. Annu Rev Neurosci 35:463–483.

Palmer L, Murayama M, Larkum M (2012) Inhibitory regulation of dendritic activity *in vivo*. Front Neural Circuits 6:26.

Paninski L (2004) Maximum likelihood estimation of cascade point-process neural encoding models. Network 15:243–262.

Pfeffer CK, Xue M, He M, Huang ZJ, Scanziani M (2013) Inhibition of inhibition in visual cortex: the logic of connections between molecularly distinct interneurons. Nat Neurosci 16:1068–1012.

Phillips EA, Hasenstaub AR (2016) Asymmetric effects of activating and inactivating cortical interneurons. Elife 5:e18383.

Pinto L, Goard MJ, Estandian D, Xu M, Kwan AC, Lee S-H, Harrison TC, Feng G, Dan Y (2013) Fast modulation of visual perception by basal forebrain cholinergic neurons. Nat Neurosci 16:1857–1863.

Pnevmatikakis EA, Soudry D, Gao Y, Machado TA, Merel J, Pfau D, Reardon T, Mu Y, Lacefield C, Yang W, Ahrens M, Bruno R, Jessell TM, Peterka DS, Yuste R, Paninski L (2016) Simultaneous denoising, deconvolution, and demixing of calcium imaging data. Neuron 89:285–299.

Pouille F, Scanziani M (2001) Enforcement of temporal fidelity in pyramidal cells by somatic feed-forward inhibition. Science 293:1159–1163.

Pouille F, Scanziani M (2004) Routing of spike series by dynamic circuits in the hippocampus. Nature 429:717–723.

Reimer J, Froudarakis E, Cadwell CR, Yatsenko D, Denfield GH, Tolias AS (2014) Pupil fluctuations track fast switching of cortical states during quiet wakefulness. Neuron 84:355–362.

Rikhye RV, Sur M (2015) Spatial correlations in natural scenes modulate response reliability in mouse visual cortex. J Neurosci 35:14661–14680.

Rudy B, Fishell G, Lee S, Hjerling-Leffler J (2011) Three groups of interneurons account for nearly 100% of neocortical GABAergic neurons. Dev Neurobiol 71:45–61.

Sebastian J, Mari Ganesh Kumar M, Sreekar YS, Rikhye RV, Sur M, Murthy HA (2017) GDspike: an accurate spike estimation algorithm from noisy calcium fluorescence signals. Paper presented at the International Conference on Acoustics, Speech and Signal Processing, New Orleans, March.

Sebastian J, Kumar MG, Viraraghavan VS, Sur M, Murthy HA (2019) Spike estimation from fluorescence signals using high-resolution property of group delay. IEEE Trans Signal Process 67:2923–2936.

Seybold BA, Phillips EAK, Schreiner CE, Hasenstaub AR (2015) Inhibitory actions unified by network integration. Neuron 87:1181–1192.

Siegle JH, Jia X, Durand S, Gale S, Bennett C, Graddis N, Heller G, Ramirez TK, Choi H, Luviano JA, Groblewski PA, Ahmed R, Arkhipov A, Bernard A, Billeh YN, Brown D, Buice MA, Cain N, Caldejon S, Casal L, et al (2021) Survey of spiking in the mouse visual system reveals functional hierarchy. Nature 592:86–92.

Softky WR, Koch C (1993) The highly irregular firing of cortical cells is inconsistent with temporal integration of random EPSPs. J Neurosci 13:334–350.

Song YH, Hwang YS, Kim K, Lee HR, Kim JH, Maclachlan C, Dubois A, Jung MW, Petersen CCH, Knott G, Lee SH, Lee SH (2020) Somatostatin enhances visual processing and perception by suppressing excitatory inputs to parvalbumin-positive interneurons in V1. Sci Adv 6:eaaz0517.

Sprague TC, Saproo S, Serences JT (2015) Visual attention mitigates information loss in small- and large-scale neural codes. Trends Cogn Sci 19:215–226.

Stringer C, Pachitariu M (2019) Computational processing of neural recordings from calcium imaging data. Curr Opin Neurobiol 55:22–31.

Tan Z, Hu H, Huang ZJ, Agmon A (2008) Robust but delayed thalamocortical activation of dendritic-targeting inhibitory interneurons. Proc Natl Acad Sci U S A 105:2187–2192.

Theis L, Berens P, Froudarakis E, Reimer J, Román Rosón M, Baden T, Euler T, Tolias AS, Bethge M (2016) Benchmarking spike rate inference in population calcium imaging. Neuron 90:471–482.

Tolhurst DJ, Movshon JA, Dean AF (1983) The statistical reliability of signals in single neurons in cat and monkey visual cortex. Vision Res 23:775–785.

Tremblay R, Lee S, Rudy B (2016) GABAergic Interneurons in the neocortex: from cellular properties to circuits. Neuron 91:260–292.

Vogelstein JT, Packer AM, Machado TA, Sippy T, Babadi B, Yuste R, Paninski L (2010) Fast nonnegative deconvolution for spike train inference from population calcium imaging. J Neurophysiol 104:3691–3704.

Wamsley B, Fishell G (2017) Genetic and activity-dependent mechanisms underlying interneuron diversity. Nat Rev Neurosci 18:299–309.

Wehr M, Zador AM (2003) Balanced inhibition underlies tuning and sharpens spike timing in auditory cortex. Nature 426:442–446.

Wei Z, Lin BJ, Chen TW, Daie K, Svoboda K, Druckmann S (2020) A comparison of neuronal population dynamics measured with calcium imaging and electrophysiology. PLoS Comput Biol 16:e1008198.

Willenbockel V, Sadr J, Fiset D, Horne GO, Gosselin F, Tanaka JW (2010) Controlling low-level image properties: the SHINE toolbox. Behav Res Methods 42:671–684.

Wilson NR, Runyan CA, Wang FL, Sur M (2012) Division and subtraction by distinct cortical inhibitory networks *in vivo*. Nature 488:343–348.

Yaeger CE, Ringach DL, Trachtenberg JT (2019) Neuromodulatory control of localized dendritic spiking in critical period cortex. Nature 567:100–104.

Yang GR, Murray JD, Wang X-J (2016) A dendritic disinhibitory circuit mechanism for pathway-specific gating. Nat Commun 7:1–14.

Yen S-C, Baker J, Gray CM (2007) Heterogeneity in the responses of adjacent neurons to natural stimuli in cat striate cortex. J Neurophysiol 97:1326–1341.

Zhang S, Xu M, Kamigaki T, Do JPH, Chang W-C, Jenvay S, Miyamichi K, Luo L, Dan Y (2014) Long-range and local circuits for top-down modulation of visual cortex processing. Science 345:660–665.

Zhang W-H, Wu S, Josić K, Doiron B (2020) Recurrent circuit based neural population codes for stimulus representation and inference. bioRxiv 389197. doi: 10.1101/2020.11.18.389197.

Zhu Y, Qiao W, Liu K, Zhong H, Yao H (2015) Control of response reliability by parvalbumin-expressing interneurons in visual cortex. Nat Commun 6:6802–6811.